

# Electronic Components for PV Generation Systems

Lead Guest Editor: Julio C. Rosas-Caro

Guest Editors: Juan M. Ramirez, Victor M. S. Huerta, and Johnny P. Contreras





---

# **Electronic Components for PV Generation Systems**

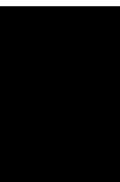
International Journal of Photoenergy

---

## **Electronic Components for PV Generation Systems**

Lead Guest Editor: Julio C. Rosas-Caro

Guest Editors: Juan M. Ramirez, Victor M. S.  
Huerta, and Johnny P. Contreras




---

Copyright © 2020 Hindawi Limited. All rights reserved.

This is a special issue published in "International Journal of Photoenergy." All articles are open access articles distributed under the Creative Commons Attribution License, which permits unrestricted use, distribution, and reproduction in any medium, provided the original work is properly cited.

# Chief Editor

Giulia Grancini , Italy

## Academic Editors




Mohamed S.A. Abdel-Mottaleb , Egypt  
Angelo Albini, Italy  
Mohammad Alghoul , Malaysia  
Alberto Álvarez-Gallegos , Mexico  
Vincenzo Augugliaro , Italy  
Detlef W. Bahnemann, Germany  
Simona Binetti, Italy  
Fabio Bisegna , Italy  
Thomas M. Brown , Italy  
Joaquim Carneiro , Portugal  
Yatendra S. Chaudhary , India  
Kok-Keong Chong , Malaysia  
Věra Cimrová , Czech Republic  
Laura Clarizia , Italy  
Gianluca Coccia , Italy  
Daniel Tudor Cotfas , Romania  
P. Davide Cozzoli , Italy  
Dionysios D. Dionysiou , USA  
Elisa Isabel Garcia-Lopez , Italy  
Wing-Kei Ho , Hong Kong  
Siamak Hoseinzadeh, Italy  
Jürgen Hüpkes , Germany  
Fayaz Hussain , Brunei Darussalam  
Mohamed Gamal Hussien , Egypt  
Adel A. Ismail, Kuwait  
Chun-Sheng Jiang, USA  
Zaiyong Jiang, China  
Yuanzuo Li , China  
Manuel Ignacio Maldonado, Spain  
Santolo Meo , Italy  
Claudio Minero, Italy  
Regina De Fátima Peralta Muniz Moreira ,  
Brazil  
Maria da Graça P. Neves , Portugal  
Tsuayoshi Ochiai , Japan  
Kei Ohkubo , Japan  
Umapada Pal, Mexico  
Dillip K. Panda, USA  
Carlo Renno , Italy  
Francesco Riganti-Fulginei , Italy  
Leonardo Sandrolini , Italy  
Jinn Kong Sheu , Taiwan  
Kishore Sridharan , India

Elias Stathatos , Greece  
Jegadesan Subbiah , Australia  
Chaofan Sun , China  
K. R. Justin Thomas , India  
Koray Ulgen , Turkey  
Ahmad Umar, Saudi Arabia  
Qiliang Wang , China  
Xuxu Wang, China  
Huiqing Wen , China  
Wei jie Yang , China  
Jiangbo Yu , USA

## Contents


---

### **L vs. LCL Filter for Photovoltaic Grid-Connected Inverter: A Reliability Study**

Ignacio Villanueva, Nimrod Vázquez , Joaquín Vaquero , Claudia Hernández, Héctor López , and Rene Osorio

Research Article (10 pages), Article ID 7872916, Volume 2020 (2020)

### **Solar Charge Controller with Maximum Power Point Tracking for Low-Power Solar Applications**

Tomy Abuzairi , Wing Wira Adimas Ramadhan, and Kresna Devara

Research Article (11 pages), Article ID 5026464, Volume 2019 (2019)

### **High-Performance Emulator for Fixed Photovoltaic Panels**

Youssef Mallal , Lhoussain El Bahir , and Touria Hassboun 

Research Article (11 pages), Article ID 3951841, Volume 2019 (2019)

## Research Article

# L vs. LCL Filter for Photovoltaic Grid-Connected Inverter: A Reliability Study

Ignacio Villanueva,<sup>1</sup> Nimrod Vázquez ,<sup>1</sup> Joaquín Vaquero ,<sup>2</sup> Claudia Hernández,<sup>1</sup> Héctor López ,<sup>1</sup> and Rene Osorio<sup>3</sup>

<sup>1</sup>Electronics Engineering Department, Tecnológico Nacional de México - IT Celaya, 38010 Celaya, Guanajuato, Mexico

<sup>2</sup>Electronics Technology Area, Universidad Rey Juan Carlos, 28933 Mostoles, Madrid, Spain

<sup>3</sup>Computer Science and Engineering Department, University of Guadalajara, 46600 Ameca, Jalisco, Mexico

Correspondence should be addressed to Nimrod Vázquez; [n.vazquez@ieee.org](mailto:n.vazquez@ieee.org)

Received 17 October 2019; Accepted 4 January 2020; Published 29 January 2020

Guest Editor: Johnny P. Contreras

Copyright © 2020 Ignacio Villanueva et al. This is an open access article distributed under the Creative Commons Attribution License, which permits unrestricted use, distribution, and reproduction in any medium, provided the original work is properly cited.

The increasing use of photovoltaic systems entails the use of new technologies to improve the efficiency and power quality of the grid. System performance is constantly increasing, but its reliability decreases due to factors such as the uncontrolled operation, the quality of the design and quantity of components, and the use of nonlinear loads that may lead to distortion in the signal, which directly affects the life of the system globally. This article presents an analysis of the reliability of a single-phase full-bridge inverter for active power injection into the grid, which considers the inverter stage with its coupling stage. A comparison between an L filter and an LCL filter, which comprise the coupling stage, is made. Reliability prediction is based on metrics, failure rate, mean time between failures, and total harmonic distortion. The analysis and numerical simulation are performed. Finally, filter considerations are suggested to extend the reliability of the inverter in a photovoltaic system.

## 1. Introduction

Nowadays exists a global concern about the excessive use of fossil energies and the environmental conditions caused by them. In recent years, global demand for electric energy has been constantly increasing, giving the opportunity for environmentally friendly energy alternatives, commonly known as renewable energy, for example, wind and solar energy; this last one is the most important due to solar irradiation on the planet [1, 2].

The photovoltaic systems have different stages of energy conversion and coupling to the electric grid, being complex and robust systems due to the big number of power semiconductors that are used [2]. The power converters are one of the weakest stages in terms of the useful life of photovoltaic systems; generally, a photovoltaic panel has a useful life in terms of reliability of 20 to 30 years, and the inverter is required to have a comparable useful life [3, 4]. This problem has been

corrected replacing the inverter when it is needed, but economically is not viable, and the repair tends to be complex; this has carried to the search for solutions to extend the life of the system as a whole [4].

For the conversion stage, different factors influence the longevity and reliability of the inverters, such as the operating ranges, the operating environment, functioning temperature, and working times. All these directly affect the useful life of the semiconductor elements and the whole photovoltaic system [5]. The most susceptible device to fail is the MOS-FET, presenting two fault states: open circuit and short circuit; another element is the diode, which is affected by electrical and thermomechanical stress. To correct these problems, materials, such as silicon carbide, are used, because of their higher voltage operating limits and lower switching losses. Also, cooling techniques and system designs are taking into account the conditions and the operating environment [6, 7].

Photovoltaic system performance may be affected for different aspects, such as deterioration of the waveforms causing harmonics and, therefore, reducing the power factor due to nonlinear loads. This is already being studied using control techniques with active or passive components for the grid injection stage [8]. Passive filters also affect the performance; they are conformed by components like inductors and capacitors. These filters have the main disadvantage in their size that may generate resonance problems if they work below the cutoff frequency. However, they present a small number of elements and are more robust [9].

Previous studies present strategies for the selection and improvement of the reliability of the converter. The authors in [7, 10, 11] propose to implement fault-tolerant converters; they perform diverse tests and compare results to different prototypes of the same converter. Some other authors, like in [4, 12], perform the analysis following the traditional method at the component level and, later, at the system level. The MIL HDBK 217 standard is used and a hybrid model for the calculation of the mean time between failure metrics. The research in [7, 13] focuses on methods based on the mission profile of the system, considering different active and inactive work phases at different temperature conditions observed by the system. Researches in [3, 14] represent systems analytically by means of logic gates and fault tree or “pareto” analysis considering a voltage component failure. Finally, in [15, 16], the Markov model is used for repairable systems using different failure and repair modes. All these previous works did not focus on the coupling stage, the passive filter, which certainly will affect the reliability of the photovoltaic system.

In this paper, a reliability study of a photovoltaic inverter is made to analyze and predict its useful life based on the probability of failures occurrences. The MIL HDBK 217F standard is used and a simulation is performed using the PSIM simulation software. The system is comprised of a full-bridge inverter, with an L or an LCL filter as the coupling stage; the objective is to determine which filter is recommended to extend the reliability and useful life of the system. Simulation results are presented as well as the system analysis using the standard mentioned before. A discussion based on the filter is made to improve the reliability of the photovoltaic system.

The document is organized as follows: first, a theoretical part is addressed, like reliability concept and the reliability standard; second, the power stage is addressed and the reliability analysis; as the third point, the simulation and discussion of proposals are made; and as the last part, the conclusions are presented.

## 2. Theoretical Aspects

To understand the analysis and proposal, some theoretical aspects are addressed first, but there are also some assumptions.

**2.1. Reliability.** Reliability describes the probability of survival of different complex electronic systems and is defined as the property that a component has to satisfactorily per-

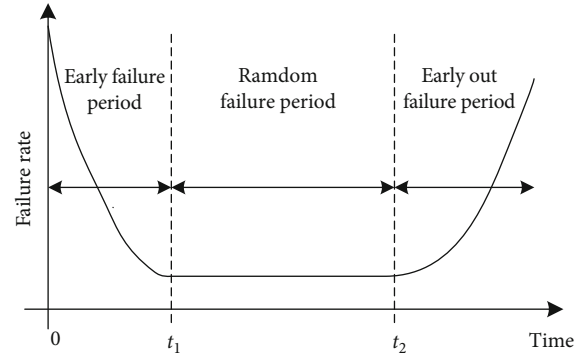


FIGURE 1: Typical risk ratio curve (bathtub).

form its function for which it was designed, for a specific time, under specific experimental conditions [6, 7]. Reliability is represented as  $R(t)$  and given by

$$R(t) = P(T > t) = 1 - F(t) = \int_0^t f(t)dt, \quad (1)$$

where  $f(t)$  is a failure density function,  $t$  is the time that the component will fail,  $F(t)$  is the cumulative distribution function, and  $P$  is the probability function.

The reliability is represented as the value that reaches the random variable  $R$  in  $t \in [0, \infty]$ ; this is the area under the density function curve, which determines the probability that the component will fail at specific time  $t$ .

When an electronic component presents a risk, it is called the failure rate, denoted by  $\lambda(t)$ , and represents the probability per unit of time that the component will survive at  $t + \Delta t$  since it already has survived for a time  $t$ . This variable is defined by [6, 14]

$$\lambda(t) = \lim_{\Delta t \rightarrow 0} \frac{f(t + \Delta t) - f(t)}{\Delta t} * \frac{1}{R(t)}, \quad (2)$$

$$\lambda(t) = \frac{F'(t)}{R(t)} = \frac{f(t)}{1 - F(t)} = \frac{f(t)}{R(t)},$$

where  $f(t)$  is the density function up to time  $t$  and  $f(t + \Delta t)$  is the density function up to time  $t + \Delta t$ .

The failure rate is variable and depends on the time of use.

The failure rate has three stages, which are represented by the bathtub curve (Figure 1), and depicts the life of a component. This curve shows an early failure period during  $t \in [0, t_1]$ ; this is caused by poor design and low-quality control. The random or constant failure period is defined by  $t \in [t_1, t_2]$ ; this means that the failure may occur at any time during that period, due to poor operating conditions and variations on the installations. Finally, the wear failure period during  $t \in [t_2, \infty]$  shows a failure rate increase which occurs at the end of the component useful life due to wear.

When the component has survived during a time  $t \in [0, \infty]$ , it is required to know the estimated average



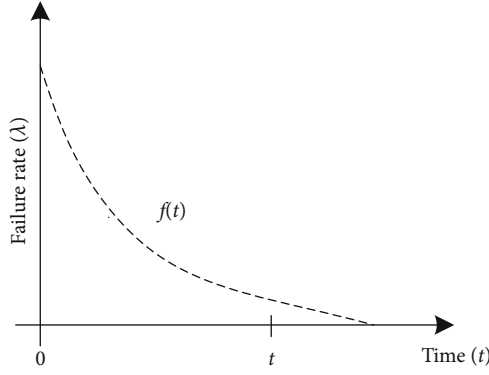
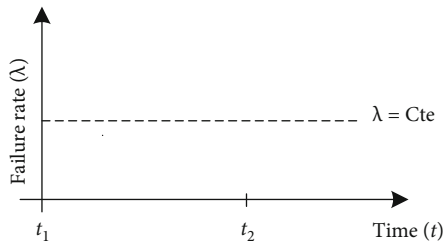
FIGURE 2: Density function  $f(t)$  of a distribution  $e(\lambda)$ .

FIGURE 3: Constant failure rate of the exponential distribution.

value of lifetime before a fault occurs, known as the mean time between failures (MTBF) and is represented by [4, 6, 14]

$$\begin{aligned} \text{MTBF} &= \int_0^{\infty} t f(t) dt, \\ \text{MTBF} &= t \cdot R(t) \Big|_0^{\infty} + \int_0^{\infty} R(t) dt = \int_0^{\infty} R(t) dt. \end{aligned} \quad (3)$$

An exponential probability distribution is used in electronic components (Figure 2), since it represents a constant failure rate (Figure 3) for devices that have exceeded the initial time with greater results  $t > 0$  and do not show wear failures.

The density function of the exponential distribution is represented by [4, 17]

$$f(t) = \lambda e^{-\lambda t}. \quad (4)$$

Integrating this equation in  $t \in [0, \infty]$  results in the cumulative distribution function of the exponential distribution:

$$F(t) = \int_0^t f(t) dt = -e^{-\lambda t}. \quad (5)$$

Substituting (5) into (1) obtained

$$R(t) = e^{-\lambda t}. \quad (6)$$

This equation is the exponential reliability function. To calculate the MTBF for the exponential distribution,

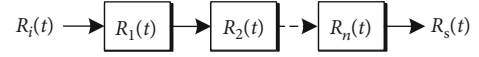


FIGURE 4: Reliability block diagram of a serial system.

(6) is substituted into (3) and is integrated, and results in [4, 6, 7, 12, 14]

$$\text{MTBF} = \int_0^{\infty} e^{-\lambda t} dt = \frac{1}{\lambda}. \quad (7)$$

**2.2. Reliability of a Serial System.** To facilitate the reliability analysis, it is done by dividing the system into subsystems. Each part of the system is represented by a block connected by arrows with other blocks of other related subsystems. Serial reliability (Figure 4) is the most practical in reliability analysis. It is said that a serial system will work properly if each block of each subsystem works as it should from  $t$  up to  $t + \Delta t$ . A serial system has a catastrophic failure when any of its subsystems fail before finishing the process.

The reliability of a serial system  $R_S(t)$  as the union of the probability of each subsystem (up to  $n$ ) is represented by

$$R_S(t) = R_1(t) \cdot R_2(t) \cdot \dots \cdot R_n(t) = \prod_{i=1}^n R_i(t). \quad (8)$$

If an exponentially distributed independent system exists, (6) is used and is substituted into (8), obtaining the following:

$$R_S(t) = e^{-(\lambda_1 + \lambda_2 + \dots + \lambda_n)t}, \quad (9)$$

where  $\lambda$  is equal to

$$\lambda = \sum_{i=1}^n \lambda_i. \quad (10)$$

Substituting (10) into (7), the MTBF is obtained for a serial system; this is

$$\text{MTBF} = \frac{1}{\lambda} = \frac{1}{\sum_{i=1}^n \lambda_i}. \quad (11)$$

If the failure rate is constant in the subsystems, the following is obtained [6, 14, 17]:

$$\text{MTBF} = \frac{1}{\lambda} = \frac{1}{n\lambda_i}. \quad (12)$$

**2.3. Standard MIL HDBK217F.** The MIL HANDBOOK 217F standard is considered to make the reliability study of the photovoltaic system, which consists of the full-bridge inverter with an L or LCL coupling filter. The standard is a prediction tool based on statistical data on tests previously performed on the components. They contain data and operating specifications of the components, physical and mathematical models that help to predict and evaluate potential failures mainly of electronic equipment.

TABLE 1: Component stress model.

Devices	Failure rate equation
Transistor	$\lambda_{PM} = \lambda_b (\pi_T \cdot \pi_A \cdot \pi_Q \cdot \pi_E)$
Inductor	$\lambda_{PI} = \lambda_b (\pi_Q \cdot \pi_E \cdot \pi_T)$
Capacitor	$\lambda_{PC} = \lambda_b (\pi_T \cdot \pi_C \cdot \pi_V \cdot \pi_{SR} \cdot \pi_Q \cdot \pi_E)$

TABLE 2: Arrhenius model.

Devices	Temperature factor
Transistor	$\pi_T = \exp(-1925(1/T_j + 273 - 1/298))$
Inductor	$\pi_T = \exp(-0.11/0.00008617)(1/T_{HS} + 273 - 1/298)$
Capacitor	$\pi_T = \exp(-0.15/0.00008617)(1/T_a + 273 - 1/298)$

A model called component stress is used to obtain the analysis factors, such as component type, component quality, operating temperature, working environment, and component failure rate, among others. The mathematical model for the component stress analysis is [5, 12, 18]:

$$\lambda_p = \lambda_b (\pi_T \cdot \pi_S \cdot \pi_C \cdot \pi_Q \cdot \pi_E \cdot \pi_A \cdot \pi_{CV}), \quad (13)$$

where  $\lambda_p$  is the failure rate of the component,  $\lambda_b$  is the base failure rate of the component,  $\pi_T$  is the encapsulation temperature factor,  $\pi_S$  is the electrical stress factor,  $\pi_C$  is the construction factor,  $\pi_Q$  is the quality factor,  $\pi_E$  is the environmental factor,  $\pi_A$  is the application factor, and finally  $\pi_{CV}$  is the capacitance factor.

In Table 1, the component stress models are shown for the elements that conform to the power stage, which are the transistor, inductor, and capacitor [5, 12, 16, 18].

As it can be observed in Table 1, the capacitor failure rate depends on the electrical stress factor  $\pi_V$ , which is a function of the stress voltage ( $V_S$ ), and this is determined by [12]

$$V_S = \frac{V_a}{V_n}, \quad (14)$$

where  $V_a$  is the applied voltage and  $V_n$  is the nominal capacitor voltage.

It is noted that for all the component models, the failure rate depends directly on the temperature factor  $\pi_T$ , which indicates the acceleration ratio taking into account the previous temperature and the temperature in accelerated conditions (Table 2). And this is directly related to the power losses; for example, switching losses are calculated to obtain the junction temperature  $T_j$ , and this is calculated with [7, 12, 16]

$$T_j = T_C + (\theta_{jc} \cdot P_{loss}), \quad (15)$$

where  $\theta_{jc}$  is the thermal resistance junction case,  $P_{loss}$  is the switch losses, and  $T_C$  is the case temperature.

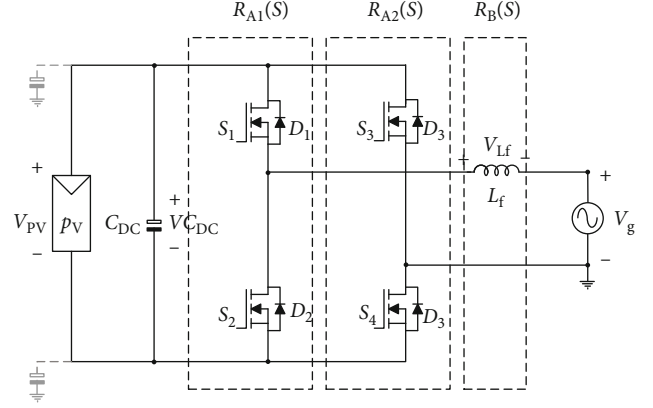


FIGURE 5: Full bridge with coupling L filter.

The MOSFET losses are determined by

$$\begin{aligned} P_{loss(static)} &= R_{DSon} \cdot I_{rms}^2, \\ P_{loss(dynamic)} &= V_{avg} \cdot I_{avg} \cdot (t_{on} + t_{off}) \cdot f_{sw}, \\ P_{loss} &= P_{loss(static)} + P_{loss(dynamic)}, \end{aligned} \quad (16)$$

where  $P_{loss}$  is the total losses,  $R_{DSon}$  is the internal resistance,  $I_{rms}$  represents the effective current,  $I_{avg}$  and  $V_{avg}$  are the average values,  $t_{on} + t_{off}$  are the on and off times, and finally  $f_{sw}$  is the switching frequency.

For the inductor, the hot spot temperature,  $T_{HS}$ , is used, and for the capacitor, the ambient temperature,  $T_a$ , is utilized [7, 12, 16, 18]:

$$T_{HS} = T_a + 1 \cdot \Delta T_d, \quad (17)$$

where  $\Delta T_d$  is the ambient temperature change.

### 3. Power Stage and Design

The power stage considered is a full-bridge inverter, rated for 1 kW, and two alternatives of passive filters are analyzed. For case 1, an L filter is used (Figure 5) and, for case 2, an LCL filter (Figure 6).

The full-bridge inverter consists of two legs composed of two switches each one; they may be operated with bipolar or unipolar PWM modulation; MOSFETs were considered. In the paper, for both cases, a unipolar modulation is used. This type of modulation allows for greater efficiency and smaller filter size and value. Having a smaller filter will impact directly on losses, which will be lower, and then reliability will be bigger.

**3.1. Filter Design: Case 1.** For the L filter design, the inductor  $L_f$  is considered a series inductance with a parasitic resistance. The L filter represents a first-order low-pass filter with a cutoff frequency of  $\omega_L = R/L$  [19].

Resonance frequency  $f_{res}$  is usually considered 10 times higher than the network frequency ( $f_o$ ) and 10 times

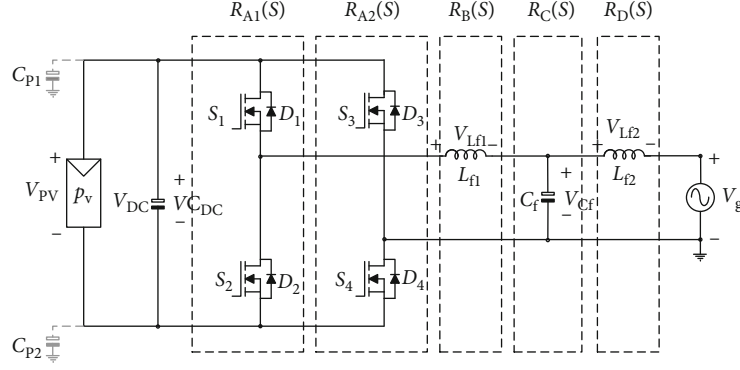


FIGURE 6: Full bridge with coupling LCL filter.

lower than the switching frequency ( $f_{sw}$ ), as it is shown next:

$$10f_o \leq f_{res} \leq f_{sw}. \quad (18)$$

**3.2. Filter Design: Case 2.** For the design of the LCL filter, two inductors are considered ( $L_{f1}$  and  $L_{f2}$ ) and a capacitor.

The inverter output voltage is a function of the photovoltaic panel voltage  $V_{pv}$  and the modulation index of the inverter  $m$ :

$$V_{Cf} = V_{pv}m. \quad (19)$$

The inverter operates with a unipolar modulation which results in lower filter size, and then considering the positive voltage of the inverter, the inductor  $L_{f1}$  can be calculated by using [20]

$$L_{f1} = \frac{V_{pv}(1-m)m}{\Delta_{iL_{f1}}f_{sw}}, \quad (20)$$

where  $\Delta_{iL_{f1}}$  is the current ripple in the inductor and  $f_{sw}$  is the switching frequency.

To obtain  $L_{f2}$ , the next equation is used [8, 19]:

$$L_{f1} = \alpha L_{f2}, \quad (21)$$

where  $\alpha$  is the ratio of the inductances.

The ratio  $\alpha$  is selected between the interval  $\alpha \in [3, 7]$ . The capacitor is selected using (18) and considering  $\omega_{res}$  as the resonant frequency, which is determined by [20, 21]:

$$C_f = \frac{L_{f1} + L_{f2}}{L_{f1}L_{f2}\omega_{res}}. \quad (22)$$

Table 3 shows the design parameters of the inverter and the filter, which were obtained using the previous equations.

**3.3. Reliability Design.** The reliability analysis is made for the system considering both filters. Then, considering first the full-bridge inverter with an L filter (Figure 5) and applying the serial reliability configuration (Figure 4), the reliability

TABLE 3: Design parameters.

L filter	LCL filter
$P_o = 1 \text{ kW}$	$P_o = 1 \text{ kW}$
$V_g = 127 \text{ Vrms}$	$V_g = 127 \text{ Vrms}$
$V_{pv} = 200 \text{ V}$	$V_{pv} = 200 \text{ V}$
$L_f = 2.4 \text{ mH}$	$L_{f1} = 425 \mu\text{H}$
	$L_{f2} = 85 \mu\text{H}$
	$C_f = 9.9 \text{ nF}$

analysis can be performed by using equations (8), (9), (10), (11), and (12).

The reliability block diagram is shown in Figure 7(a), and it is the product of the reliability of the four switches and the inductor; this is

$$R_S(t) = R_{A1}(t) \cdot R_{A2}(t) \cdot R_B(t),$$

$$R_{A1}(t) = R_{S1}(t) \cdot R_{S2}(t),$$

$$R_{A2}(t) = R_{S3}(t) \cdot R_{S4}(t), \quad (23)$$

$$R_B(t) = R_{Lf}(t),$$

$$R_S(t) = R_{S1}(t) \cdot R_{S2}(t) \cdot R_{S3}(t) \cdot R_{S4}(t) \cdot R_{Lf}(t).$$

It is assumed that the reliability of the switches is  $R_{S1}(t) = R_{S2}(t) = R_{S3}(t) = R_{S4}(t)$  equal; also, a constant failure rate is presented; therefore,  $\lambda_{S1} = \lambda_{S2} = \lambda_{S3} = \lambda_{S4} = \lambda_1$ ; additionally,  $\lambda_{Lf} = \lambda_2$  which represents the inductor failure rate.

Substituting the exponential reliability function (6) into (23) gives the total system reliability depending on the failure rate of each element, as shown next:

$$R_S(t) = e^{-\lambda_1 t} \cdot e^{-\lambda_1 t} \cdot e^{-\lambda_1 t} \cdot e^{-\lambda_1 t} \cdot e^{-\lambda_2 t}, \quad (24)$$

$$R_S(t) = e^{-(4\lambda_1 + \lambda_2)t}.$$

To calculate the MTBF of the entire system, the total reliability is replaced, (24) in (3), and integrating from 0 to  $t$ ,

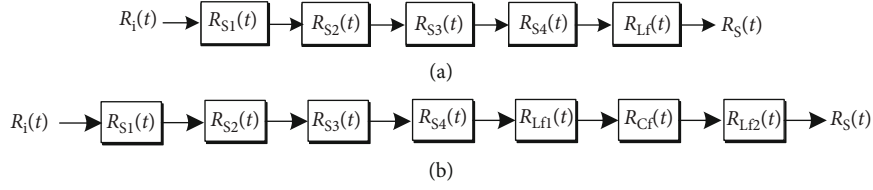


FIGURE 7: Serial block diagram of the full bridge with (a) L filter and (b) LCL filter.

when  $t = \infty$ . It can be seen that the MTBF is the inverse of the system failure rate:

$$\text{MTBF} = \frac{1}{4\lambda_1 + \lambda_2}. \quad (25)$$

The same process for the full-bridge inverter with the LCL filter (Figure 6) is performed. The reliability block diagram in series is shown in Figure 7(b), which represents the product of the reliability of each of the four switches, the two inductors, and the capacitor.

It is assumed also that  $R_{S1}(t) = R_{S2}(t) = R_{S3}(t) = R_{S4}(t)$ , and then the failure rate of the four switches is equal to  $\lambda_{S1} = \lambda_{S2} = \lambda_{S3} = \lambda_{S4} = \lambda_1$ ; the inductor fault rate is  $\lambda_{Lf1} = \lambda_2$  for the first one,  $\lambda_{Lf2} = \lambda_3$  for the second, and finally  $\lambda_{Cf} = \lambda_4$  for the capacitor. Based on the block diagram, the following is obtained:

$$\begin{aligned} R_S(t) &= R_{A1}(t) \cdot R_{A2}(t) \cdot R_B(t) \cdot R_C(t) \cdot R_D(t), \\ R_{A1}(t) &= R_{S1}(t) \cdot R_{S2}(t), \\ R_{A2}(t) &= R_{S3}(t) \cdot R_{S4}(t), \\ R_B(t) &= R_{Lf1}(t), \\ R_C(t) &= R_{Cf}(t), \\ R_D(t) &= R_{Lf2}(t), \\ R_S(t) &= R_{S1}(t) \cdot R_{S2}(t) \cdot R_{S3}(t) \cdot R_{S4}(t) \cdot R_{Lf1}(t) \cdot R_{Cf}(t) \cdot R_{Lf2}(t). \end{aligned} \quad (26)$$

The reliability of the full-bridge with the LCL filter is calculated as follows: (6) is substituted into (26) obtaining

$$\begin{aligned} R_S(t) &= e^{-\lambda_1 t} \cdot e^{-\lambda_1 t} \cdot e^{-\lambda_1 t} \cdot e^{-\lambda_1 t} \cdot e^{-\lambda_2 t} \cdot e^{-\lambda_3 t} \cdot e^{-\lambda_4 t}, \\ R_S(t) &= e^{-(4\lambda_1 + \lambda_2 + \lambda_3 + \lambda_4)t}. \end{aligned} \quad (27)$$

Substituting (27) into (3), the MTBF of the entire system is calculated as

$$\text{MTBF} = \frac{1}{4\lambda_1 + \lambda_2 + \lambda_3 + \lambda_4}. \quad (28)$$

Equations (24), (25), (27), and (28) are used in the following section to calculate the reliability and the MTBF.

## 4. Reliability Analysis of the Photovoltaic System

To make the reliability analysis, some simulations are made, but also, some data are obtained from the standard. The simulation is performed to obtain the operating parameters; these are the voltage and current that are used in the reliability models. For the capacitor, the stress voltage ( $V_S$ ) is used; on the other hand, the losses for the MOSFET ( $P_{\text{loss}}$ ) must be calculated using the steady-state values of the converter.

**4.1. Numerical Simulation Results.** The numerical simulation of the full-bridge inverter for both cases, L and LCL filters, is performed with the design parameters of Table 3. PSIM® software is used for its versatility and simulation speed. Some parameters obtained from the datasheet were added to simulation components, such as MOSFET IRF540, to get the simulation results and reliability prediction closer to reality.

In Figure 8, the simulation for the power stage considering the L filter is observed. From top to bottom, the ac main voltage (120 V<sub>rms</sub>) and the injected current (8.3 A<sub>rms</sub>) are illustrated.

Figure 9 shows the results obtained for the LCL filter; from top to bottom, the ac main voltage (120 V<sub>rms</sub>) and the injected current under the same power conditions are graphed.

In both cases, the active power corresponds to 1 kW. The current is in phase with the ac voltage; therefore, a high power factor is achieved in both cases. The total harmonic distortion (THD) is different in both cases; Table 4 shows the THD of the injected current; it can be seen that values of 0.382% and 0.00926% for the L and LCL filters are obtained, respectively. According to the above, it is better to use an LCL filter than an L filter.

It is known that the distortion of the waveform affects the quality of the signal, therefore affecting directly the reliability.

**4.2. Reliability Calculation.** The numerical calculation of reliability is performed using the traditional MIL HDBK 217F standard. It is important to note that the reliability of the inverter depends on the acceleration parameter of the test and the temperature factor.

For the application of the standard, the adjustment factors are considered, also the base failure rate, which will generate an adjustment component failure rate. The total system failure rate, the MTBF, and the overall reliability are calculated. A high ambient temperature of 35°C is considered where the system will operate.

The adjustment factors used are shown in Tables 5 and 6 for the L and LCL filters, respectively, according to the

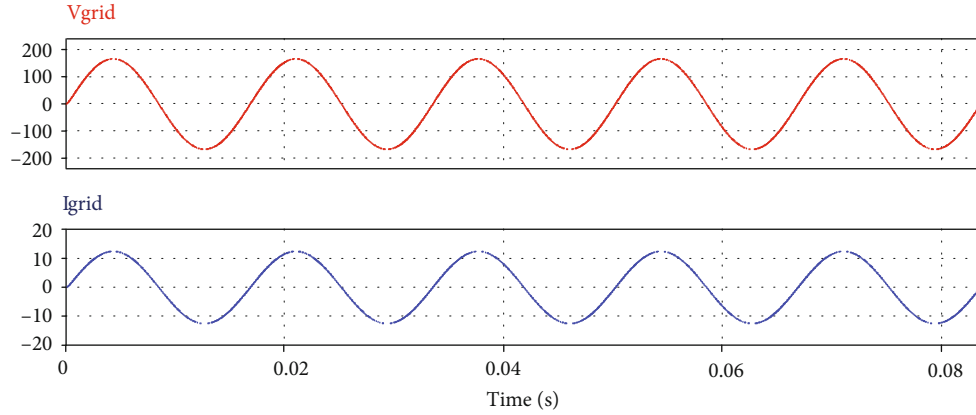


FIGURE 8: Active power injection filter with L filter. From top to bottom: average voltage (100 V/div) and average current (10 A/div).

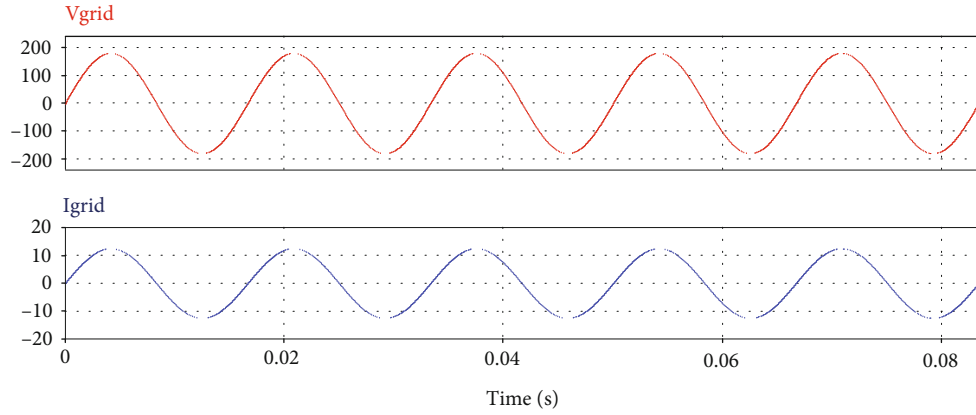


FIGURE 9: Active power injection filter with LCL. From top to bottom: average voltage (100 V/div) and average current (10 A/div).

TABLE 4: Filter L and LCL data and THD.

	$L_{f1}$	$C$	$L_{f2}$	THD
L filter	2.56 mH			0.382%
LCL filter	425 $\mu$ H	9.9 $\mu$ F	85 $\mu$ H	0.00926%

TABLE 5: L filter adjustment factors.

Device	$\lambda_b$	$\pi_T$	$\pi_A$	$\pi_Q$	$\pi_E$
MOSFET	0.012	3.68	5.5	8	6
Inductor	0.00003	1.82		3	6

TABLE 6: LCL filter adjustment factors.

Device	$\lambda_b$	$\pi_T$	$\pi_A$	$\pi_Q$	$\pi_E$	$\pi_C$	$\pi_V$
MOSFET	0.012	3.67	5.5	8	6		
Inductor	0.00003	1.82		3	6		
Capacitor	0.00037	1.209		10	10	0.35449	26.17

TABLE 7: Reliability of L filter vs. LCL filter.

Failure/ $10^6$	L	LCL
$\lambda_{PM}$ (MOSFET)	12.973	12.800
$\lambda_{PI}$ (Ls)	0.00098350	0.00098355
$\lambda_{PC}$ (C)		0.014092541
$\lambda_{System}$ (total)	51.173	51.216
MTBF	0.0195415	0.0195251

standard. The environmental factor is defined for the benign fixed terrestrial environment (GB) according to MIL HDBK 217.

The average and effective values of voltage and current are used for the calculation of losses, and these are made by using (16). The losses are used in the Arrhenius model to calculate the temperature factor  $\pi_T$  that is necessary to obtain the MOSFET adjustment failure rate.

Table 7 shows the total system failure rate and the MTBF which are expressed in failure/ $10^6$  hours. These were calculated using (24), (25), (27), and (28).

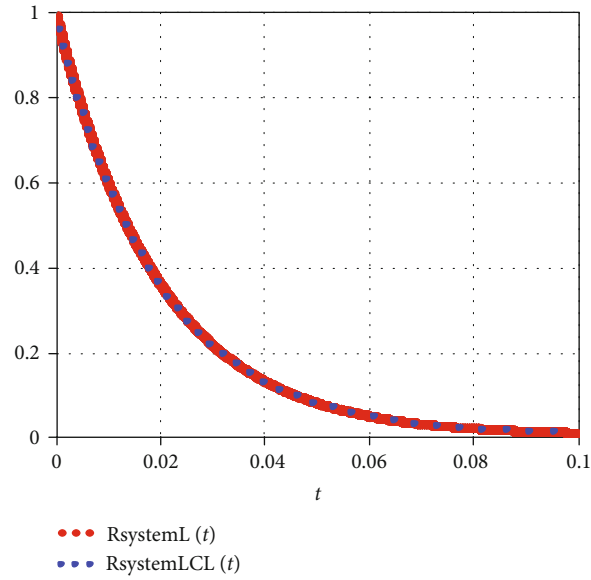


FIGURE 10: Comparison of the L and LCL filter reliability.

TABLE 8: Filter value vs. reliability.

$L_{f1}$	$\alpha$	$L_{f2}$	$C$	$\lambda_{\text{System}}$ (failure/ $10^6$ hrs)	MTBF (failure/ $10^6$ hrs)	THD
425 $\mu$ H	3	141 $\mu$ H	6.6 $\mu$ F	51.214	0.0195251	0.00910%
425 $\mu$ H	4	106 $\mu$ H	8.2 $\mu$ F	51.215	0.0195251	0.00922%
425 $\mu$ H	5	85 $\mu$ H	9.9 $\mu$ F	51.216	0.019525	0.00926%
425 $\mu$ H	6	71 $\mu$ H	11 $\mu$ F	51.216	0.019525	0.00941%
425 $\mu$ H	7	61 $\mu$ H	13 $\mu$ F	51.216	0.019525	0.00934%

In the case of the full-bridge with an L filter, the MOSFETs contribute to 99.99% of the global failure rate and the inductor 0.01%. For the full-bridge with an LCL filter, again, the greater contribution for the global failure rate is given by the MOSFETs with 99.97%, while the inductors have 0.0038% and the capacitor with 0.0261%.

It is observed that the most susceptible element to fail is the MOSFET. The reliability prediction, with the MIL HDBK 217F standard, shows that a full-bridge inverter with an L filter is more reliable since the total failure rate of the full-bridge inverter with an LCL filter is higher ( $\alpha = 5$ ); additionally, the same occurs with the MTBF, which determines the average life, and then it will be smaller. However, the reliability gain is marginal.

The decision-making, in this case, depends on the application. It should be noted that the number of elements plays a very important role in this calculation; the greater the number of the elements is, the higher the failure rate and the lower MTBF will be.

In Figure 10, the comparison of the L and LCL filter reliability is observed. The reliability is expressed in  $10^6$  hrs. The dotted line represents the reliability of the LCL filter system with  $0.0195251 \times 10^6$  hrs of life, while the straight line shows the L filter with  $0.0195415 \times 10^6$  hrs.

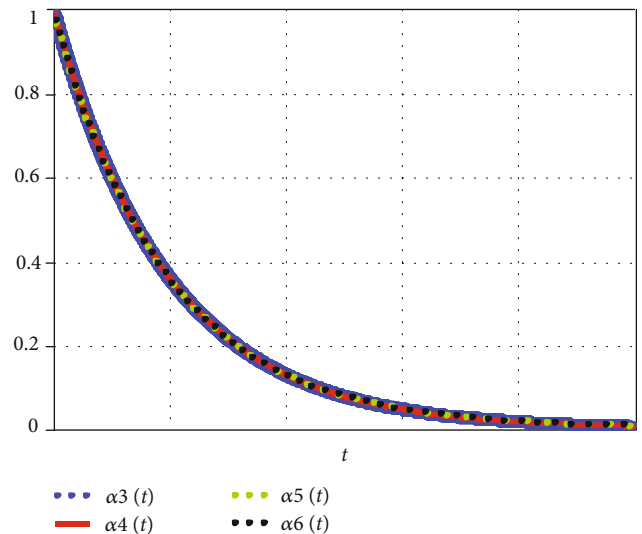


FIGURE 11: Comparison of reliability for different values of the components of the LCL filter.

The reliability difference in both cases is marginal. In the case of the LCL filter, the  $\alpha$  ratio for the filter design also affects the reliability.

TABLE 9: L and LCL filter sizes.

Filter type	Value of the passive element			Core	Passive element data		Total volume (cm <sup>3</sup> )	
	$L_{f1}$	$L_{f2}$	$C$		Core volume	Capacitor volume		
L	2.4 mH	—	—	3xETD-59	240.80 cm <sup>3</sup>		240.80	
$\alpha = 3$	425 $\mu$ H	141 $\mu$ H	6.6 $\mu$ F	ETD-54	56.8 cm <sup>3</sup>	12 cm <sup>3</sup>	92.9 cm <sup>3</sup>	
				RM-14	24.1 cm <sup>3</sup>			
$\alpha = 4$	425 $\mu$ H	106 $\mu$ H	8.2 $\mu$ F	ETD-54	56.8 cm <sup>3</sup>	12 cm <sup>3</sup>	83.5 cm <sup>3</sup>	
				RM-12	14.7 cm <sup>3</sup>			
LCL	$\alpha = 5$	425 $\mu$ H	85 $\mu$ H	9.9 $\mu$ F	ETD-54	56.8 cm <sup>3</sup>	16.12 cm <sup>3</sup>	87.7 cm <sup>3</sup>
					RM-12	14.7 cm <sup>3</sup>		
$\alpha = 6$	425 $\mu$ H	71 $\mu$ H	11 $\mu$ F	ETD-54	56.8 cm <sup>3</sup>	16.12 cm <sup>3</sup>	87.7 cm <sup>3</sup>	
				RM-12	14.7 cm <sup>3</sup>			
$\alpha = 7$	425 $\mu$ H	61 $\mu$ H	13 $\mu$ F	ETD-54	56.8 cm <sup>3</sup>	20.83 cm <sup>3</sup>	92.33 cm <sup>3</sup>	
				RM-12	14.7 cm <sup>3</sup>			

In Table 8, a comparison for different values for the LCL filter is made, based on the  $\alpha$  ratio of the filter design, which yields an effect on the reliability, MTBF, and THD. The best options are found for a ratio of three and four; with a ratio of three, a THD of 0.00910% and  $0.0195251 \times 10^6$  hours of lifespan is obtained, with 51.214 failures/ $10^6$  hrs. If the THD is smaller, the size of the second inductor increases and the capacitor value decreases, which in the end contributes to a lower failure rate increasing its useful life. As can be observed, the LCL filter with the  $\alpha$  ratio of four has the same reliability with the L filter case.

In Figure 11, the comparison of the reliability for the LCL is observed; the graph is made using different values of  $\alpha$ .

Another important factor of the ratio  $\alpha$  is the system size. Taking into account the inductor values of Table 8, the volume of the filter is calculated. In Table 9, due to the selected core and film capacitor, the volume is obtained; this is made for the L and LCL filter changing  $\alpha$ . As it can be observed, the best case for the volume is the LCL filter with a ration of four, since the size for the others is higher. It is important to notice that increasing the ratio  $\alpha$  does not imply a lower volume since the cores available are finite; this may change depending on the rated power and type of cores used.

With this analysis, it can be deduced that the LCL filter may offer reliability compared to the L filter; therefore, the LCL filter should be always preferred because a better THD is obtained. If the volume is also added in the decision process, then, the ratio  $\alpha$  must be selected properly and not necessarily high because the reliability shows that not only a lower  $\alpha$  is better, but also the volume may not decrease by increasing  $\alpha$ .

## 5. Conclusion

In this article, the prediction of the reliability of a full-bridge inverter with different coupling filters is presented. The MIL HDBK 217 standard is used to calculate the failure rate and the mean time between failures. The study showed that the devices that are most likely to fail are the MOSFETs, due to thermal and electrical stresses that they are subjected during the switching stage.

The system with the L filter has an average life greater than the LCL filter usually designed, but marginal; however, the LCL case offers the best THD. Another analysis illustrates that the system reliability with LCL coupling is affected by the ratio  $\alpha$ , resulting in the fact that a value of 3 gets the best characteristic regarding THD and reliability, even comparable with the use of the L filter.

If the volume is considered, then the ratio  $\alpha$  should be selected carefully since the higher ratio does not imply the lower volume according to the analysis; however, due to the reliability analysis and the THD obtained, the lower ratio  $\alpha$  should be preferred. Then a compromise between reliability and volume can be made; the best case is a ratio of four in the analysis presented here.

## Data Availability

The data used to support the findings of this study are included within the article.

## Conflicts of Interest

The authors declare that there is no conflict of interest regarding the publication of this paper.

## Acknowledgments

This research was partially funded by the PROMINT-CM S2018/EMT-4366 program from the Comunidad de Madrid, Spain. Also, this work was partially funded by Tecnológico Nacional de México.

## References

- [1] B. K. Bose, "Global warming: energy, environmental pollution, and the impact of power electronics," *IEEE Industrial Electronics Magazine*, vol. 4, no. 1, pp. 6–17, 2010.
- [2] A. Chakraborty, "Advancements in power electronics and drives in interface with growing renewable energy resources," *Renewable and Sustainable Energy Reviews*, vol. 15, no. 4, pp. 1816–1827, 2011.

- [3] N. Gupta, R. Garg, and P. Kumar, "Sensitivity and reliability models of a PV system connected to grid," *Renewable and Sustainable Energy Reviews*, vol. 69, pp. 188–196, 2017.
- [4] A. Ristow, M. Begovic, A. Pregelj, and A. Rohatgi, "Development of a methodology for improving photovoltaic inverter reliability," *IEEE Transactions on Industrial Electronics*, vol. 55, no. 7, pp. 2581–2592, 2008.
- [5] S. Harb and R. S. Balog, "Reliability of candidate photovoltaic module-integrated-inverter (PV-MII) topologies—a usage model approach," *IEEE Transactions on Power Electronics*, vol. 28, no. 6, pp. 3019–3027, 2013.
- [6] F. Richardeau and T. T. L. Pham, "Reliability calculation of multilevel converters: theory and applications," *IEEE Transactions on Industrial Electronics*, vol. 60, no. 10, pp. 4225–4233, 2013.
- [7] S. E. De León-Aldaco, H. Calleja, F. Chan, and H. R. Jiménez-Grajales, "Effect of the mission profile on the reliability of a power converter aimed at photovoltaic applications—a case study," *IEEE Transactions on Power Electronics*, vol. 28, no. 6, pp. 2998–3007, 2013.
- [8] P. Channegowda and V. John, "Filter optimization for grid interactive voltage source inverters," *IEEE Transactions on Industrial Electronics*, vol. 57, no. 12, pp. 4106–4114, 2010.
- [9] J. Wu, H. Jou, Y. Feng, W. Hsu, M. Huang, and W. Hou, "Novel circuit topology for three-phase active power filter," *IEEE Transactions on Power Delivery*, vol. 22, no. 1, pp. 444–449, 2007.
- [10] V. V. S. Pradeep Kumar and B. G. Fernandes, "A fault-tolerant single-phase grid-connected inverter topology with enhanced reliability for solar PV applications," *IEEE Journal of Emerging and Selected Topics in Power Electronics*, vol. 5, no. 3, pp. 1254–1262, 2017.
- [11] U. Choi, F. Blaabjerg, and K. Lee, "Reliability improvement of a T-type three-level inverter with fault-tolerant control strategy," *IEEE Transactions on Power Electronics*, vol. 30, no. 5, pp. 2660–2673, 2015.
- [12] F. Chan and H. Calleja, "Reliability estimation of three single-phase topologies in grid-connected PV systems," *IEEE Transactions on Industrial Electronics*, vol. 58, no. 7, pp. 2683–2689, 2011.
- [13] Y. Yang, H. Wang, and F. Blaabjerg, "Reliability assessment of transformerless PV inverters considering mission profiles," *International Journal of Photoenergy*, vol. 2015, Article ID 968269, 10 pages, 2015.
- [14] Y. Song and B. Wang, "Survey on reliability of power electronic systems," *IEEE Transactions on Power Electronics*, vol. 28, no. 1, pp. 591–604, 2013.
- [15] A. K. Barnes, J. C. Balda, and A. Escobar-Mejía, "A semi-Markov model for control of energy storage in utility grids and microgrids with PV generation," *IEEE Transactions on Sustainable Energy*, vol. 6, no. 2, pp. 546–556, 2015.
- [16] F. H. Aghdam and M. Abapour, "Reliability and cost analysis of multistage boost converters connected to PV panels," *IEEE Journal of Photovoltaics*, vol. 6, no. 4, pp. 981–989, 2016.
- [17] "IEEE recommended practice for the design of reliable industrial and commercial power systems," *IEEE Std 493-2007 (Revision of IEEE Std 493-1997)*, pp. 1–383, 2007.
- [18] "Reliability prediction of electronic equipment," *Military Handbook 217F, US Department of Defense*, 1995, Notice 2, December 1991 (Superseding).
- [19] Y. Noh, B. Choi, S. Lee, J. Eom, and C. Won, "An optimal method to design a trap-CL filter for a PV AC-module based on flyback inverter," *IEEE Transactions on Industry Applications*, vol. 52, no. 2, pp. 1632–1641, 2015.
- [20] F. Liu, X. Zha, Y. Zhou, and S. Duan, "Design and research on parameter of LCL filter in three-phase grid-connected inverter," *2009 IEEE 6th International Power Electronics and Motion Control Conference*, pp. 2174–2177, 2009.
- [21] S. Jayalath and M. Hanif, "Generalized LCL-filter design algorithm for grid-connected voltage-source inverter," *IEEE Transactions on Industrial Electronics*, vol. 64, no. 3, pp. 1905–1915, 2017.



## Research Article

# Solar Charge Controller with Maximum Power Point Tracking for Low-Power Solar Applications

**Tomy Abuzairi** , **Wing Wira Adimas Ramadhan**, and **Kresna Devara**

*Department of Electrical Engineering, Faculty of Engineering, Universitas Indonesia, Depok, West Java 16424, Indonesia*

Correspondence should be addressed to Tomy Abuzairi; [tomy.abuzairi@gmail.com](mailto:tomy.abuzairi@gmail.com)

Received 11 October 2019; Accepted 18 November 2019; Published 16 December 2019

Guest Editor: Julio C. Rosas-Caro

Copyright © 2019 Tomy Abuzairi et al. This is an open access article distributed under the Creative Commons Attribution License, which permits unrestricted use, distribution, and reproduction in any medium, provided the original work is properly cited.

Solar Charge Controller (SCC) with Maximum Power Point Tracking (MPPT) is needed to extract maximum energy from photovoltaic. However, a SCC device with MPPT technology feature is expensive on the market due to the requirements for a high-power system. On the other hand, in lower power applications such as IoT sensors, solar street lights, and wireless communication nodes, these types of controllers can be produced at a lower cost. In this study, the design of a low-cost SCC was conducted using the MPPT technology for low-power solar applications. The SCC is designed based on the Arduino microcontroller, which has the role of controlling the circuit and producing PWM signals to regulate the DC-DC converter. Several tests were conducted to validate the efficiency of the MPPT algorithm. The SCC device succeeded in increasing efficiency up to 52% on the low irradiance level.

## 1. Introduction

Nowadays, renewable energy is very popular, and it is growing very rapidly in various applications, such as microgrids [1], nanogrids, smart converter [2], and Internet of Things (IoT) devices [3]. This growth of solar module use is due to the reduction of module cost, because of the manufacturing process advancing and the increased demand for green energy [4]. Although the solar module is starting to be widely used, in its utilization, there are a number of challenges and limitations. One of them is the power properties of the solar module relating to the load that follows the characteristics of the  $P$ - $V$  module [5]. As a solution to this problem, a Solar Charge Controller (SCC) with Maximum Power Point Tracking (MPPT) is needed to extract maximum energy from the solar module [6]. The MPPT not only increase the system's output power but also give the system a longer lifespan [7].

MPPT algorithms are designed so that the system can adapt to weather changes and achieve optimal power. Therefore, several algorithms can be utilized, such as open-circuit voltage, short-circuit current, incremental conductance, and P&O (Perturb and Observation) [8]. These algorithms are integrated into the power electronic components, where their

duty cycle is controlled to deliver the maximum available power to the load [9, 10]. The MPPT applied a buck converter and Pulse Width Modulation (PWM) signal to keep the load from the module and the load balanced, so the module's output power reaches the maximum [11].

Currently, SCC device with MPPT on the market is expensive due to the requirements for a high-power system. However, in lower power applications such as IoT sensors, solar street lights, and wireless communication nodes, these types of controllers can be produced at a lower cost. In this study, low-cost SCC with MPPT technology for low-power solar application was developed. The controller used a microcontroller board from Arduino Nano to monitor the module and battery and generate the PWM signal [12]. Arduino Nanos use an ATmega328p chip with simple components, so the price is relatively cheap [13]. The SCC was implemented in a lower power solar module with the lithium-ion batteries as a load.

## 2. Photovoltaic Characteristics

The photovoltaic is a semiconductor that produces electricity by converting energy from sun irradiance to electricity [5]. Photovoltaic performance is dependent on the current

weather, insolation, temperature, and other surroundings. The common basic external influences of photovoltaic power performance are insolation or irradiance and temperature of the device [14]. Figures 1(a) and 1(b) show the illustration of the power-voltage characteristic curve and current-voltage characteristic curve generated by the photovoltaic, along with the changes in irradiance and temperature.

Figure 1(a) shows that the power-voltage curve generated will be shifted to the right with decreasing temperature, causing the module to generate a higher voltage, while the increase of irradiance affects both the power generated and voltage generated, causing these values to increase [14]. Figure 1(b) shows that the current-voltage curve generated will shift to the right with decreasing temperature, the same as in Figure 1(a). The increase of irradiance affects both the current generated and the maximum voltage generated, causing that these values will also increase [14]. These ambient parameters, such as temperature and insolation, are affected by the surrounding conditions, such as the geographical aspect, weather, and altitude.

Following these characteristics, the photovoltaic needs to operate at its maximum voltage value to avoid power loss. The maximum voltage value is the voltage when the photovoltaic produces its maximum power point and is marked by the red dot in Figure 1. Because of this condition, using a load with an impedance that does not match the impedance of photovoltaic will cause power loss. Therefore, to optimize the photovoltaic power, the system can harness MPPT technology.

### 3. MPPT Technology

Maximum Power Point Tracking or MPPT is a technology that can control a power source from photovoltaic, such as a solar module, to generate its maximum power [11]. MPPT uses a DC-DC converter to control the solar module for charging the lithium-ion battery, as shown in Figure 2. This DC-DC converter then needs to operate using a certain algorithm, so the power of the solar module reaches the maximum point. Control of the DC-DC converter can be undertaken by controlling the PWM signal that drives the DC-DC converter, following various tracking algorithms, such as Perturb and Observation (P&O). For MPPT to conduct the tracking algorithm, MPPT needs a controller device or circuit that can monitor the solar module conditions, such as the voltage, current, and temperature. The controller for MPPT should have the capability to sense at least one data measurement of the solar module conditions, then control or produce the duty cycle needed by the PWM signal to drive the DC-DC converter.

**3.1. DC-DC Converter.** A DC-DC converter consists of several types of circuit, such as buck converter, boost converter, and cuk converter. A buck converter is a circuit that is used to reduce the input voltage of the buck converter circuit so that it is lower than the input at the output side [15]. Figure 3 shows a basic asynchronous buck converter circuit. A buck converter used an inductor connected series between the input and the output; a switching element

connected series between the input and inductor, an output capacitor; and a diode connected parallel to the circuit ground between the switch and the inductor, an input capacitor.

For the buck converter to operate, the input has to be connected and opened periodically [6]. Thus, the buck converter has two steps of operation. The first step is the closed circuit, and the next is the opened circuit step. Figure 4(a) shows the short-circuit step when the switch element is closed; this condition causes the input to power the load and charge the inductor and output capacitor [15]. After the inductor and the output capacitor are charged, the second step will occur. Figure 4(b) shows the second step, when the switch is opened. In the second step, the charged inductor powers the load in this step [15]. These two steps will be repeated as long as the buck converter is operating. To implement this process, the circuit uses a transistor component as a switching element controlled by a PWM signal. By changing the duty cycle of the PWM signal, the duration time of the closed circuit step in the period will change, and thus, the solar module voltage will change correspondingly to the duty cycle value of the PWM signal.

**3.2. Perturb and Observation Algorithm.** The Perturb and Observation (P&O) algorithm is a tracking technique algorithm used in MPPT to achieve maximum power by perturbing the power source and observing the impact [11]. There are various MPPT algorithms, such as fuzzy logic [16] and particle swarm optimization [17]. However, P&O is the most used technique in an MPPT system because it has a simple algorithm and does not require a high capability controller device [11]. The first step of the P&O algorithm is measuring the voltage and current of the solar module, then calculating the current value and the difference between the current voltage and power against voltage and power measured from the previous loop. The controller then decides, from the difference value, whether to increase or decrease the voltage of the solar module by changing the duty cycle of the PWM signal so that the power of the solar module will increase.

**3.3. Lithium-Ion Battery Charging Technique.** The lithium-ion battery (LIB) is the most commonly used battery in electrical products and devices [18]. They have been used in almost all portable devices in the fields of communication, power, and data processing. Even though LIB is known for their durability, they have a procedure for charging and discharging. LIB are known to explode if the usage does not correspond to their profile [18]. Constant-current and constant-voltage (CC-CV) is one of the charging techniques that can be implemented on an LIB. The purpose of CC-CV is to maximize the charging and the lifetime of the battery [19].

Figure 5 shows the charging procedure of CC-CV of a single LIB. CC-CV consists of four stages of charging [19]. The first stage is trickle and happens when the battery voltage is below 3 V; in this condition, the charging current must be below 0.1 C. C is the labeled capacity of the battery used. When the battery voltage is above 3 V and below 4.2 V, the

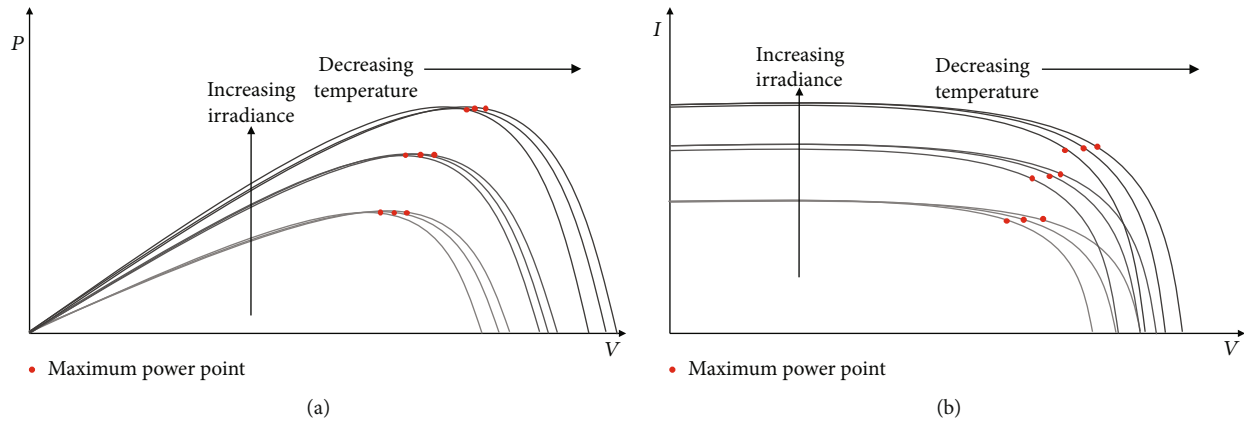


FIGURE 1: Illustration of photovoltaic characteristics under different irradiance and temperature: (a) power-voltage characteristic curve; (b) current-voltage characteristic curve.

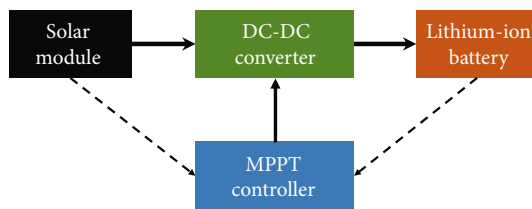


FIGURE 2: Block diagram of a basic SCC device.

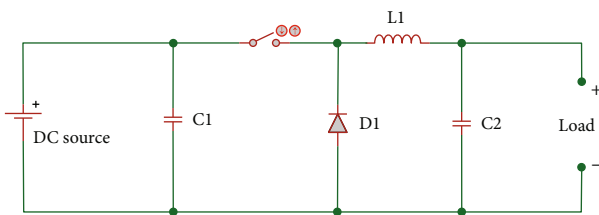


FIGURE 3: An asynchronous buck converter circuit.

battery enters the second stage of charging, the constant current. The constant current stage is charging the battery from 0.2C to 1C in a constant or semiconstant charging current. The third stage is the constant voltage stage, where the battery voltage is above 4.2V; then, the current must slowly reduce so that the battery voltage is below or equal to 4.2V. The last stage, end of charge, occurs when the charging current falls below 0.02C, indicating that the charging is finished and the current can be cut.

#### 4. Design of SCC

Figure 6 shows the block diagram of the designed SCC. The designed SCC utilized a buck converter circuit to control the solar module power. The SCC controller used a microcontroller Arduino Nano to monitor the solar module power and Li-ion battery, using two INA219 sensors. An INA219 is a power sensor IC manufactured by Texas Instrument [20]. The battery used was two cells connected in parallel; therefore, the battery was treated as a single cell with 4200mAh of total capacity. The display OLED was used by the Arduino

Nano to display the power measured on both the solar module and the battery. The Arduino Nano was powered from the battery using a step-up 5V circuit due to the single-cell Li-ion battery voltage being lower than the Arduino Nano operating voltage.

Figure 7 shows the electric schematic of the designed SCC device. S1 and S2 are I-V sensor INA219 for the solar module and single-cell Li-ion battery power sensor, respectively. J1 is the connector to the solar module. The step-up circuit used MT3608 IC to produce 5V [21]. The feedback resistor of R2 and R3 had to have a certain value of resistance to give the appropriate voltage drop value. R2 and R3 resistance values should be high enough that the current is small enough; then, the power loss will be reduced. The buck converter followed the basic buck converter circuit, but the switching element used a series of resistor, NPN transistor, and a MOSFET, instead of just using a single MOSFET. The switching element components are marked by Q1, Q2, and R1.

**4.1. Buck Converter and Solar Module.** The buck converter circuit was designed so that the circuit operated on Continuous Current Mode (CCM) on every tested PWM frequency. CCM is an operating condition under which the current in the inductor (L1) never reaches zero while operating. The tested frequencies were 23kHz, 62.5kHz, 92kHz, and 186kHz. The inductor value needs to correspond to the circuit parameter so that the CCM can be achieved.  $L_a$  and  $L_b$ , respectively, from Equations (1) and (2), were used to determine the minimal value of the inductance needed; the value must exceed both  $L_a$  and  $L_b$  [15, 22, 23]. To find the values of  $L_a$  and  $L_b$ , we need to know the circuit parameters, such as the maximum and minimum voltage of the input and output of the circuit, minimum frequency of the PWM signal, maximum ripple current, and minimum current. The maximum current can be obtained by dividing the maximum power of the solar module used ( $P_{mp}$ ) by the minimum output voltage ( $V_{out_{min}}$ ) following the solar module specification shown in Table 1 and the load voltage, respectively. The solar module used in this experiment was SUNLITE, with a maximum peak power ( $P_{mp}$ ) of 10 W.

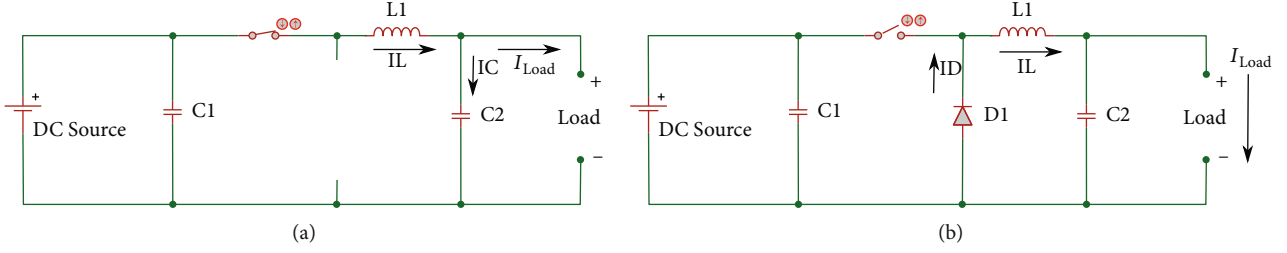


FIGURE 4: Two steps of buck converter operation: (a) closed circuit step; (b) opened circuit step.

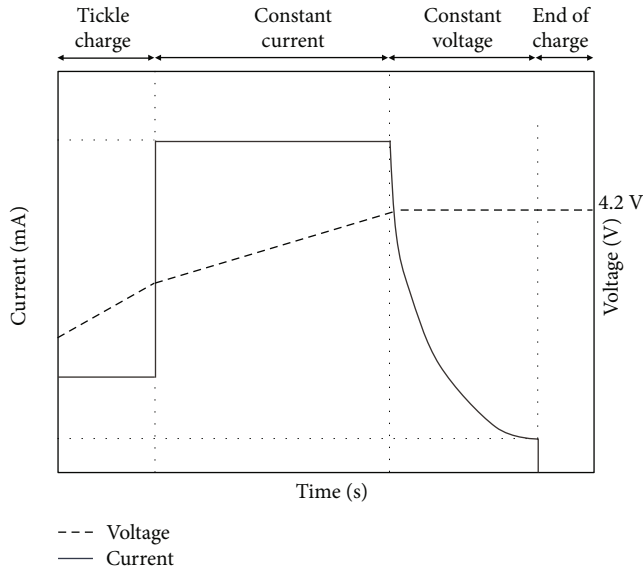


FIGURE 5: Constant-current and constant-voltage charging procedure for single-cell Li-ion batteries.

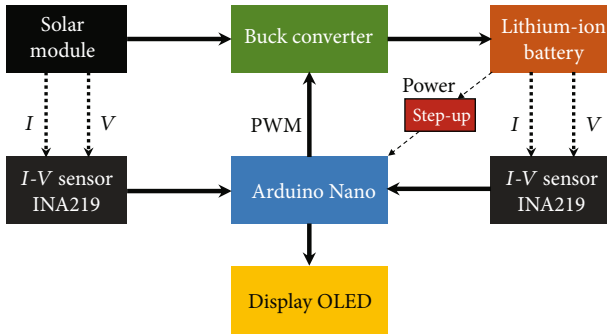


FIGURE 6: Block diagram of the designed SCC device.

Thus, the maximum current was obtained by a value of 3.3 A. The minimum frequency of the PWM signal ( $F_s$ ) was 23 kHz. Following the Texas instrument guide, the maximum ripple should be 20% of the maximum current; thus, the maximum ripple ( $\Delta I L_{\max}$ ) was obtained by a value of 660 mA [22]. The minimum current of the buck converter follows the single-cell Li-ion battery minimum charging current or 2% of the battery capacity [19]. The capacity of the battery used was 4200 mA. By replacing the variables in the

circuit parameters, we obtained the largest value of both inductance values by  $836 \mu\text{H}$ . Thus, the inductance chosen for  $L_1$  was  $1000 \mu\text{H}$ . This  $L_1$  value was chosen because it exceeds  $L_a$  and  $L_b$  and to anticipate additional ripple current caused by Equivalent Resistant Series (ESR) by the inductor:

$$L_a = \frac{V_{\text{out}_{\max}} (1 - (V_{\text{out}_{\max}}/V_{\text{in}_{\max}}))}{2 F_{s_{\min}} I_{\text{out}_{\min}}}, \quad (1)$$

$$L_b = \frac{V_{\text{out}_{\max}} (1 - (V_{\text{out}_{\max}}/V_{\text{in}_{\max}}))}{(F_{s_{\min}} \Delta I L_{\max})}. \quad (2)$$

$C_2$  is the output capacitor that used to reduce the voltage ripple on the output side [22]. The ripple occurred because of the fundamental operation of the buck converter that opened and closed the circuit periodically, causing the voltage to ripple. The maximum ripple ( $\Delta V_{\text{out}_{\min}}$ ) was 5 mV on the load or output side; to achieve this ripple, a capacitor was applied on the load side, labelled as  $C_2$ . Equation (3) was used to obtain the minimum value of the capacitor needed [22, 23]. By replacing the maximum current ( $\Delta I L_{\max}$ ), minimum frequency ( $F_{s_{\min}}$ ), and maximum voltage ( $\Delta V_{\text{out}_{\min}}$ ), we obtained the minimum capacitance ( $C_{\text{out}_{\min}}$ ) value of  $273 \mu\text{F}$ . The value of  $C_2$  capacitance was  $470 \mu\text{F}$ . The  $C_2$  value was chosen because the value exceeds the minimum and to anticipate the ESR. A lower capacitance value was used as long as the value is exceeded and additional ripple caused by the ESR is still below the circuit standard or design. The capacitor specifications must be considered, such as the maximum operating voltage, so that the solar module voltage never exceeds the capability of the capacitor operation voltage:

$$C_{\text{out}_{\min}} = \frac{\Delta I L_{\max}}{F_{s_{\min}} \Delta V_{\text{out}_{\min}}}, \quad (3)$$

The switching element component utilized a series of resistors ( $R_1$ ), NPN transistor ( $Q_2$ ), and power MOSFET ( $Q_1$ ).  $R_1$  and  $Q_2$  were used to amplify the PWM signal voltage. The amplified PWM was generated as a voltage drop between  $R_1$  and  $Q_1$ . The voltage drop was applied to drive the gate of the MOSFET; therefore, the MOSFET's capability to conduct current was maximized [24, 25].  $10 \text{ k}\Omega$  was applied for  $R_1$ , so the current flow through  $R_1$  was minimized and the power loss reduced;  $R_1$  may be applied using a lower or higher value as long as the transistor off state condition can still produce a high enough voltage to drive the MOSFET; thus, the MOSFET effective gate voltage should be below the amplified

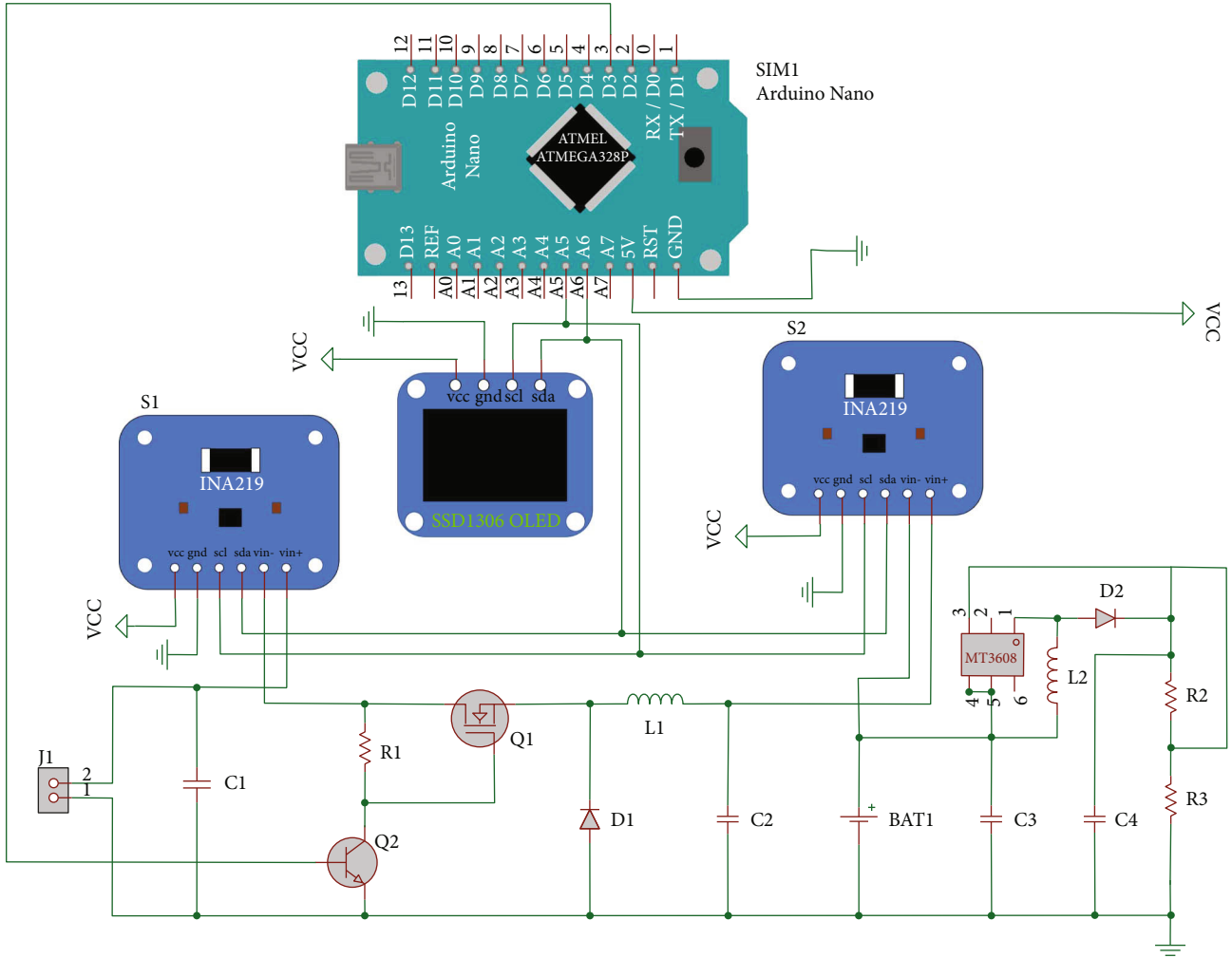


FIGURE 7: Electrical schematic of the designed SCC device.

TABLE 1: Specifications of the solar module.

Maximum power ( $M_P$ )	10 W
Voltage at maximum power ( $V_{MP}$ )	18.36 V
Current at maximum power ( $I_{MP}$ )	0.54 A
Open-circuit voltage ( $V_{oc}$ )	22.00 V
Short-circuit current ( $I_{sc}$ )	0.58 A

PWM signal highest voltage. The NPN transistor used was 2N because of its ability to process 250 kHz signal, matched with the circuit operation [26]. The power MOSFET for Q1 was AOD444 because its switching time is faster than a common power MOSFET, such as the IRF series, and it has the same capability for power as the IRF series.

**4.2. MPPT Algorithm.** The designed MPPT algorithm was developed from basic P&O value tracking with adaptations and limitations for Arduino implementation. Figure 8 shows the flowchart of the designed MPPT algorithm. To find the maximum power point, first, the Arduino of the device must measure the solar module current voltage and current, then

calculate the difference between the present power against the previous power ( $\Delta P$ ) and the present voltage against the previous voltage ( $\Delta V$ ). The Arduino then decides from the difference calculation whether the present power generated is on the left side or the right side of the present condition of the maximum power point (MPP). If both the  $\Delta P$  and  $\Delta V$  values are below zero, the current power is on the left side of the MPP; therefore, the voltage of the solar module must be increased and vice versa. Generating a higher solar module voltage can be achieved by increasing the duty cycle value. Because the Arduino cannot limit its own duty cycle value by itself, a duty cycle tracking limit is implemented. When the device decides to increase the duty cycle value, the Arduino has to decide whether the current value is already 100%. If the condition is met, the duty cycle needs to be reduced instead of increasing the value and vice versa if the current duty cycle value is already 0%.

**4.3. Charging Controller Algorithm.** The charging controller algorithm utilized basic constant-current (CC) and constant-voltage (CV) for Li-ion battery charging. Figure 9 shows the designed algorithm of the implemented CC-CV,

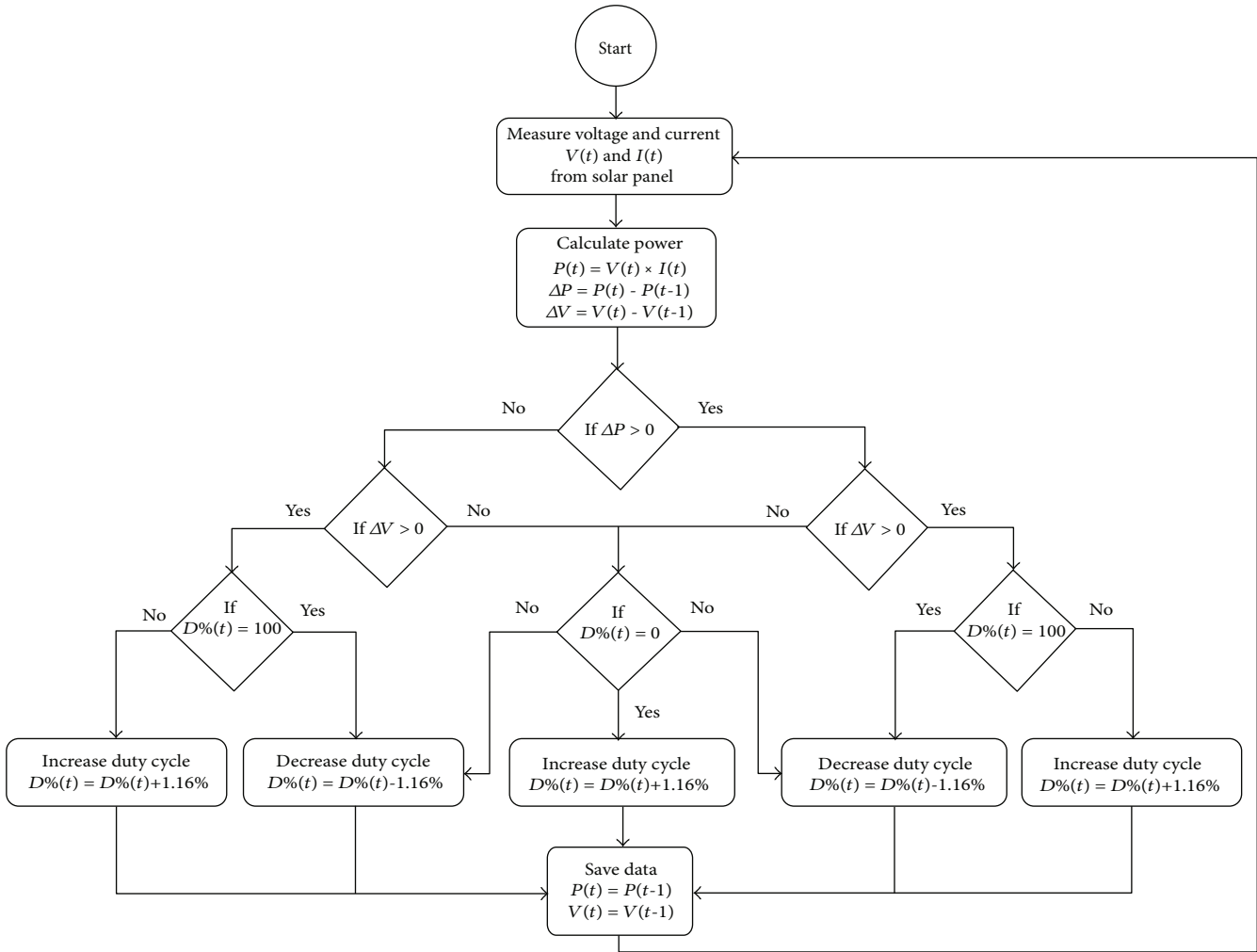


FIGURE 8: Flow chart of the designed MPPT algorithm.

with the inclusion of the MPPT algorithm and the utilized Li-ion battery specification. Before initiating any charging current, the device must cut off the current by setting the duty cycle value ( $D\%$ ) by 100%. Then, the Arduino measures the battery characteristic and decides the battery charging step. For increasing  $D\%$  in Arduino, 1.16% was applied rather than 1% due to limitation on high-frequency PWM in Arduino [27].

The first charging step that must be evaluated is trickle charging; if the battery is below 3 V and the current is, respectively, below 0.1 C or 420 mA, corresponding to the design, the charging must be maintained at a maximum of 420 mA. If the battery then rises above 3 V while the current is still below 420 mA, the battery is ready to enter the second step. The second step is CC that charges when the battery is above 3 V and below 4.2 V. The charging current can be maximized to 1 C or 4200 mA, corresponding to the design, and the suggested current should be constant or semiconstant. When the battery reaches 4.2 V, the battery has entered the third stage, CV. The CV stage functions to maintain the battery voltage at 4.2 V by reducing the current progressively. The last step is the end of charge; when the charging current

reaches 0.02 C or 84 mA, cutting off the charging current will be performed, and thus, the battery will finish charging.

## 5. Results and Discussion

**5.1. Solar Module Power Test.** To vary the irradiance of the solar module, a Phillip 500 W Halogen Lamp and variable transformer were used. The test was conducted by connecting 5 k $\Omega$  and changing the value by turning the knob of the potentiometer, while the lighting was applied to the solar module using the halogen lamp. Figure 10 shows the  $I$ - $V$  curve and  $P$ - $V$  curve generated by using three different irradiance values: 400 W/m<sup>2</sup>, 200 W/m<sup>2</sup>, and 80 W/m<sup>2</sup>. These results were used to validate the device performance by referring to the solar module power test result.

**5.2. Buck Converter MULTISIM Simulation Results.** To ascertain the ability of the designed buck converter to control the power of the solar module, circuit simulation was performed on MULTISIM. MULTISIM is an electric circuit simulation program using SPICE [28]. The simulation applied the same buck converter circuit as shown in

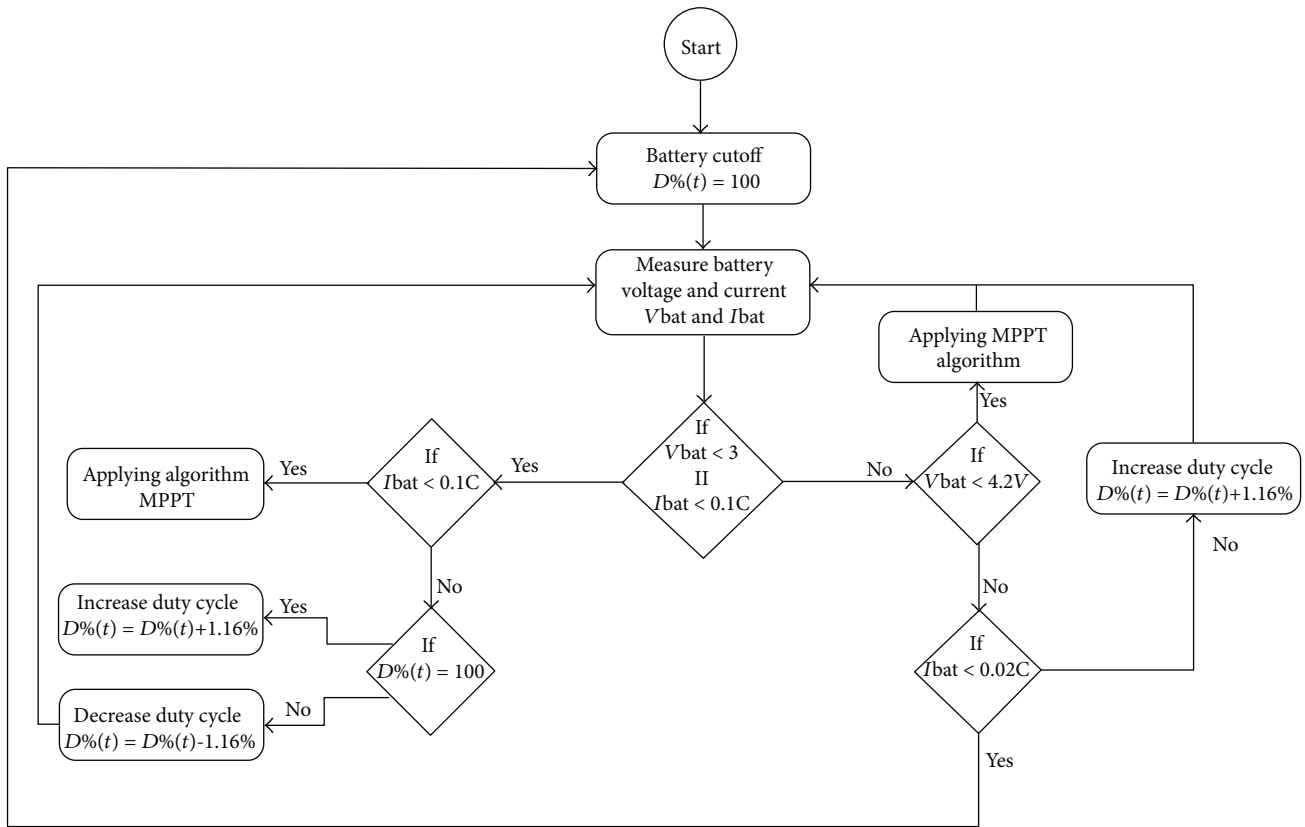


FIGURE 9: Flow chart of the designed charging control algorithm.

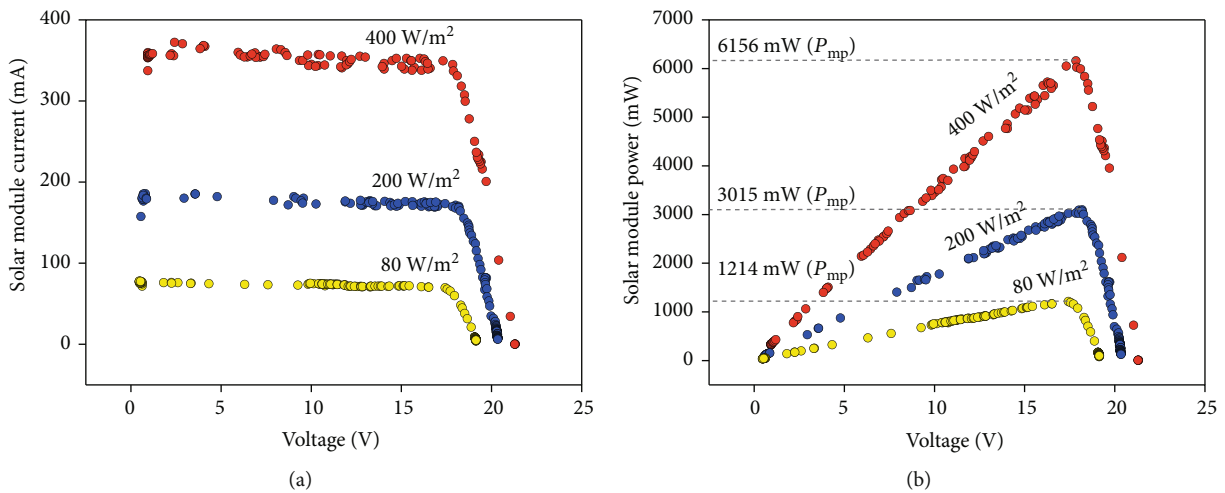


FIGURE 10: Power test result of the solar module: (a)  $I$ - $V$  curve; (b)  $P$ - $V$  curve.

Figure 7, using corresponding components such as C1, C2, R1, Q1, Q2, D1, L1, and BAT1. Because the AOD444 MOSFET model is not available in MULTISIM, IRF540 was used as a substitution for MOSFET AOD444, as it has the same N-channel type and the fastest switching of the IRF series, with suitable operation specifications available in MULTISIM. To simulate the solar module in the simulation, the current limited source with the voltage of maximum power

voltage from the module was applied. The frequencies applied were 23 kHz, 62.5 kHz, 92 kHz, and 186 kHz, corresponding to Arduino’s ability to produce a PWM signal with 1.16% as the largest duty cycle step [27].

Figure 11(a) depicts the changes of the solar module voltage or input voltage along with the duty cycle value. It shows that the higher the duty cycle value, the greater the increase of the solar module voltage. These changes show

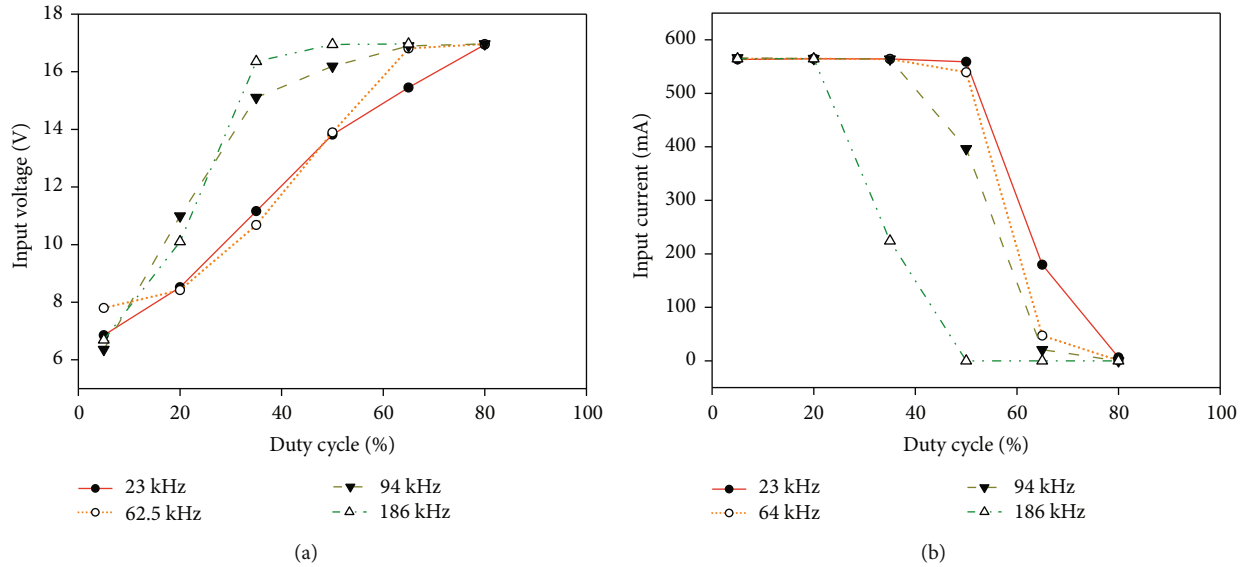


FIGURE 11: Solar module voltage and current behavior: (a) input voltage vs. DC; (b) input current vs. DC.

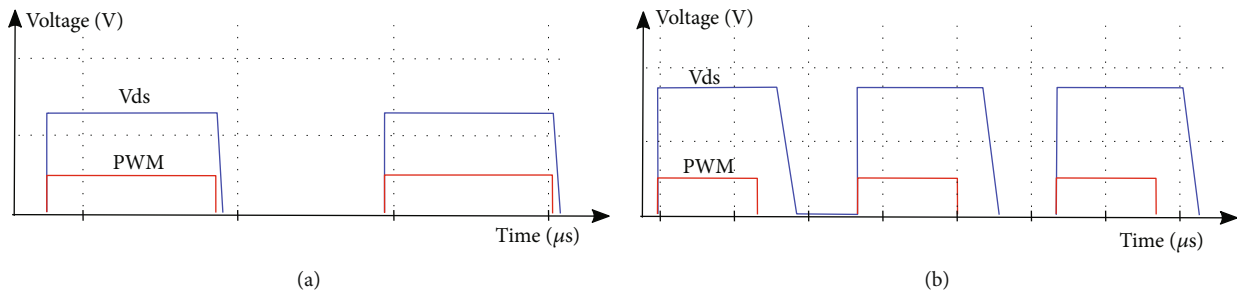


FIGURE 12:  $V_{ds}$  and PWM signals: (a) 23 kHz; (b) 186 kHz.

that the buck converter can manipulate the solar module voltage and show that the voltage and duty cycle are positively correlated, indicating that the circuit configuration and especially the switching elements are working properly. Figure 11(b) shows the changes of the solar module current or input current against the duty cycle value; the current will rise, then at some point will start reducing and reach cut-off. This behavior is the same for the solar module current-voltage characteristics; thus, the buck converter can be used on an MPPT device. Although there is a match between the behavior of the data and the design, the plots in Figures 11(a) and 11(b) experienced shifting with the increase of frequency. In Figures 11(a) and 11(b), a higher frequency makes the plots shift more to the left. This behavior occurred due to the delay of the switching capability of the MOSFET [23].

Figure 12(a) shows the  $V_{ds}$  and PWM voltage signals on 23 kHz operation; the  $V_{ds}$  signal shows a delay against the PWM signal changes, but this is not significant. Figure 12(b) shows the  $V_{ds}$  and PWM signals on 186 kHz operation, demonstrating a significant delay between the  $V_{ds}$  and PWM voltage signal. This indicates that the MOSFET is operating on a constant or semiconstant delay; thus, the increase of the frequency makes the difference more significant.

**5.3. Buck Converter Circuit Test.** The designed buck converter circuit was tested using  $400 \text{ W/m}^2$  irradiance. Figure 13 shows the results of the buck converter test. Figure 13(a) depicts the changes of the solar module voltage or input voltage along with the duty cycle value, and Figure 13(b) depicts the changes of the solar module current or input current along with the duty cycle value. Overall, the behavior matched the MULTISIM simulation results, but the plot experienced more shifting along with the increase of frequency. This was assumed to be because of the MOSFET delay, inductive load, and perfect calculated conditions on the MULTISIM causing more shifting instead of the same shifting or less. Aside from this phenomenon, these results show that the buck converter circuit can be used for an SCC device. The most efficient frequency was 23 kHz from among the other tested frequencies, due to the 23 kHz duty cycle range of operation being the widest and having the most insignificant switching delay against the operating PWM frequency; thus, the device used a 23 kHz PWM signal.

**5.4. MPPT Tracking Test.** To validate the MPPT algorithm in the SCC device, two tests were conducted on the prototype of SCC device. The first test was conducted by applying three levels of irradiances,  $400 \text{ W/m}^2$ ,



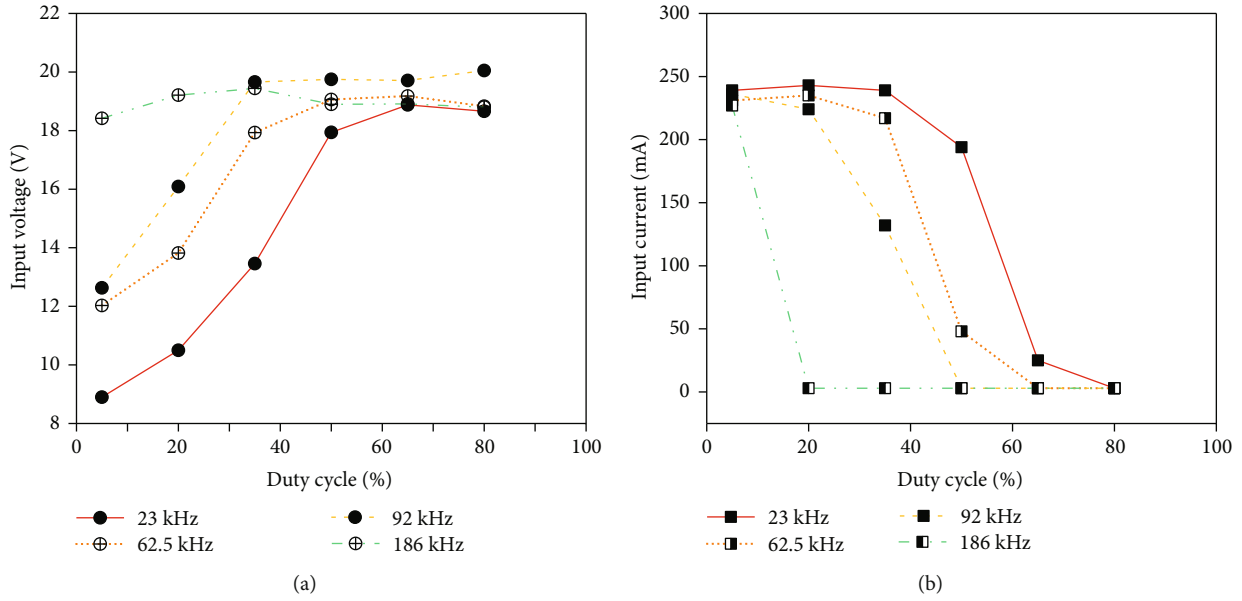


FIGURE 13: Power test result of the designed buck converter circuit using a halogen lamp: (a) input voltage vs. duty cycle; (b) input current vs. duty cycle.

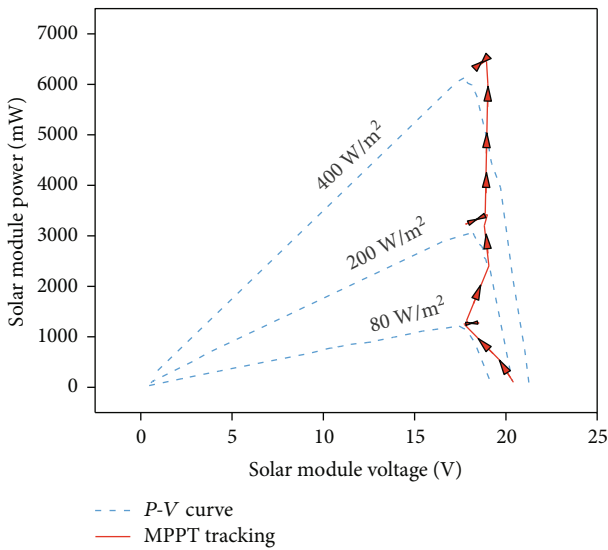


FIGURE 14: Designed MPPT tracking result.

200 W/m<sup>2</sup>, and 80 W/m<sup>2</sup>, continuously to vary the P-V curve that would be tracked by the device. Figure 14 shows the MPPT tracking results, with the P-V curve shown in Figure 10 as the tracking reference. The test was conducted by applying the irradiance gradually from 80 W/m<sup>2</sup>, 200 W/m<sup>2</sup>, and 400 W/m<sup>2</sup> as the device managed to achieve the maximum power. The results show that the MPPT was correct for tracking from the open voltage condition to the maximum power point. As the irradiance value increased, tracking moved to the new maximum power point. Because of these behaviors, it can be concluded that the designed MPPT is appropriate to the P-V characteristic curve and MPPT purpose.

TABLE 2: Tracking speed test results of MPPT.

Duty cycle starting point	Time to maximum power point (ms)		
	80 W/m <sup>2</sup>	200 W/m <sup>2</sup>	400 W/m <sup>2</sup>
100%	936	659	481
80%	387	373	438
60%	0	10	53
40%	144	221	498
20%	464	703	727
0%	742	937	1343

The second MPPT test was to observe the tracking speed, as shown in Table 2. Different irradiance and duty cycle tracking starting points were varied separately instead of continuously, as in the first test. Table 2 shows the time as the device started to track, until the maximum power point was achieved. The fastest tracking time was achieved with 60% duty cycle starting point in the three different irradiance values. Therefore, we utilized 60% as the duty cycle starting point in this MPPT.

**5.5. Charging Controller Test.** To test the charging controller capability of the SCC device, charging a battery using the device was conducted. The battery charging finishes in six hours, and the results are shown in Figure 15. As the simulation of the solar module, ADITEG APS-3005 was used to generate the identical power specification of maximum power that can be generated by the solar module.

Figure 15 shows that all four stages of CC-CV were implemented by the device. The trickle charge was completed and is shown in Figure 15(a). For the first charging period, the current was below 420 mA and the voltage was below 3 V, as in Figure 15(b). Then, the current rose and varied

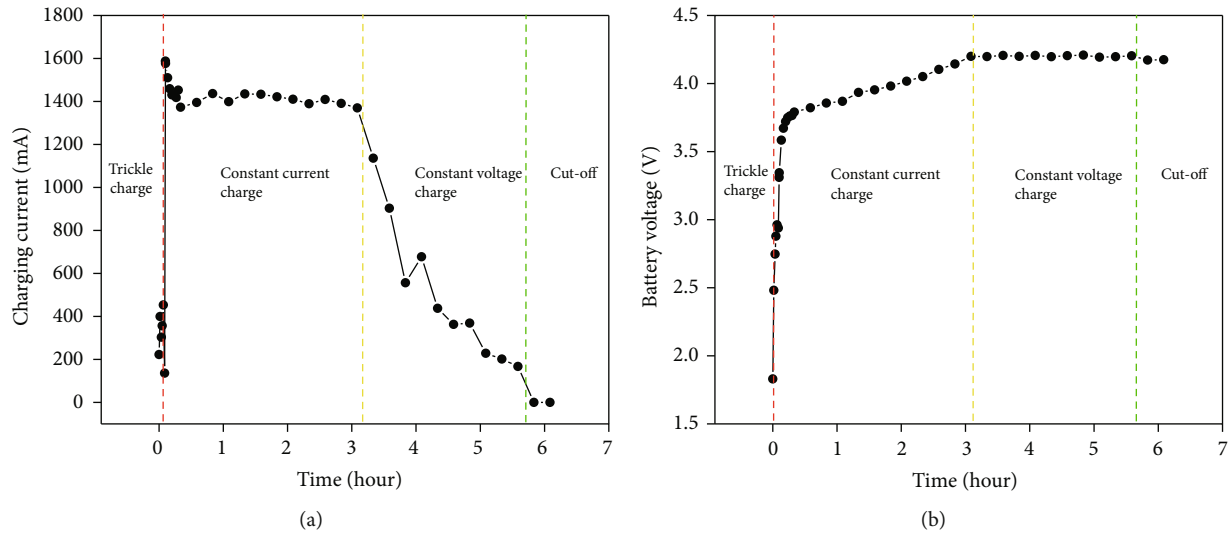


FIGURE 15: Charging controller test result: (a) charging current vs. time; (b) battery voltage vs. time.

TABLE 3: Efficiency test result with MPPT and without MPPT.

Irradiance	Efficiency		
	Without MPPT	With MPPT	Improvement
80 W/m <sup>2</sup>	26%	78%	52%
200 W/m <sup>2</sup>	27%	73%	46%
400 W/m <sup>2</sup>	29%	68%	39%

from 1400 to 1600 mA, and the battery voltage was below 4.2 V and above 3 V, indicating that the CC charging was successfully performed. When the battery voltage rose to 4.2 V, the current started to reduce gradually, as shown on the CV charge. The last stage is end of charge or cut-off, indicated by the charging current reaching zero and the current, before reaching zero, already being low, indicating that the battery finished its charging. Although on the last stage the battery voltage was 4.18 V, meaning that charging could actually still be performed, it was assumed that the device was charging the battery with a low current again; thus, the battery would be expected to rise again to 4.2 V. Therefore, the cut-off was performed; then, the battery voltage decreased a little but was higher than before, and the cycle continued until the battery reached 4.2 V and did not decrease again.

**5.6. Efficiency Test.** The efficiency test was conducted using a solar module powered by a halogen lamp. The three irradiance values of 80 W/m<sup>2</sup>, 200 W/m<sup>2</sup>, and 400 W/m<sup>2</sup> were applied. The tested device was with the MPPT and without the MPPT technology. Table 3 shows the efficiency with the MPPT and without the MPPT under different irradiance values. The highest increase in efficiency was 52% at 80 W/m<sup>2</sup>, while the lowest increase in efficiency was 39% at 400 W/m<sup>2</sup>. This behavior occurred because in the SCC device without the MPPT, the solar module voltage was dropped to the load voltage, while the current flow had the same value as

in the MPPT, while with the MPPT, the voltage of the solar module stayed at its maximum value. Therefore, the efficiency of the device without MPPT was much lower due to significant power loss relative to the solar module's maximum power.

## 6. Conclusions

Overall, the designed SCC with MPPT technology was able to manage maximum power tracking and control battery charging. The designed MPPT managed to utilize the solar module more efficiently than a system that did not use MPPT. The designed buck converter was able to sweep along the  $P$ - $V$  curve of the solar module. The use of the frequency of the buck converter PWM driving signal must be considered, as the MOSFET used has performance issues, such as delay of the switching, which could cause additional power loss and narrowing of the operating range of the buck converter. Arduino Nano can be used as the PWM generator and as a charging controller using CC-CV. The frequency of the PWM produced by Arduino and the duty cycle step are correlated; thus, the value must be considered to correspond to the design and needs. The MPPT managed to achieve the highest efficiency of 78% while without MPPT, only 26% was achieved.

## Data Availability

All data used to support the findings of this study are included within the article.

## Conflicts of Interest

The authors declare that they have no conflicts of interest.

## Acknowledgments

This research was supported by the QQ Research Grant 2019 (No. NKB-0327/UN2.R3.1/HKP.05.00/2019) from Universitas Indonesia.

## References

- [1] A. Anvari-Moghaddam, J. M. Guerrero, J. C. Vasquez, H. Monsef, and A. Rahimi-Kian, "Efficient energy management for a grid-tied residential microgrid," *IET Generation, Transmission & Distribution*, vol. 11, no. 11, pp. 2752–2761, 2017.
- [2] M. Merenda, D. Iero, G. Pangallo et al., "Open-source hardware platforms for smart converters with cloud connectivity," *Electronics*, vol. 8, no. 3, p. 367, 2019.
- [3] N. Sahraei, S. Watson, S. Sofia, A. Pennes, T. Buonassisi, and I. M. Peters, "Persistent and adaptive power system for solar powered sensors of Internet of Things (IoT)," *Energy Procedia*, vol. 143, pp. 739–741, 2017.
- [4] G. Kavлак, J. McNerney, and J. E. Trancik, "Evaluating the causes of cost reduction in photovoltaic modules," *Energy Policy*, vol. 123, pp. 700–710, 2018.
- [5] M. A. Green, *Solar Cells: Operating Principles*, Prentice-Hall, Englewood Cliff, NJ, USA, 1982.
- [6] N. Onat, "Recent developments in maximum power point tracking technologies for photovoltaic systems," *International Journal of Photoenergy*, vol. 2010, Article ID 245316, 11 pages, 2010.
- [7] L. Gil-Antonio, B. Saldivar, O. Portillo-Rodríguez, J. C. Ávila-Vilchis, P. R. Martínez-Rodríguez, and R. Martínez-Méndez, "Flatness-based control for the maximum power point tracking in a photovoltaic system," *Energies*, vol. 12, no. 10, p. 1843, 2019.
- [8] N. Karami, N. Moubayed, and R. Outbib, "General review and classification of different MPPT techniques," *Renewable and Sustainable Energy Reviews*, vol. 68, pp. 1–18, 2017.
- [9] S. L. Brunton, C. W. Rowley, S. R. Kulkarni, and C. Clarkson, "Maximum power point tracking for photovoltaic optimization using ripple-based extremum seeking control," *IEEE Transactions on Power Electronics*, vol. 25, no. 10, pp. 2531–2540, 2010.
- [10] R. A. Mastromauro, M. Liserre, T. Kerekes, and A. Dell'Aquila, "A single-phase voltage-controlled grid-connected photovoltaic system with power quality conditioner functionality," *IEEE Transactions on Industrial Electronics*, vol. 56, no. 11, pp. 4436–4444, 2009.
- [11] A. M. Atallah, A. Y. Abdelaziz, and R. S. Jumaah, "Implementation of perturb and observe MPPT of PV system with direct control method using buck and buck-boost converters," *Emerging Trends in Electrical, Electronics & Instrumentation Engineering: An international Journal*, vol. 1, no. 1, pp. 31–44, 2014.
- [12] Arduino, "What is Arduino?," April 2019, <https://arduino.cc>.
- [13] Arduino, "Arduino Nano," August 2019, <https://store.arduino.cc/usa/arduino-nano>.
- [14] M. H. Moradi and A. R. Reisi, "A hybrid maximum power point tracking method for photovoltaic systems," *Solar Energy*, vol. 85, no. 11, pp. 2965–2976, 2011.
- [15] R. W. Erickson and D. Maksimovic, *Fundamentals of Power Electronics*, Kluwer Academic, Norwell, MA, USA, 2001.
- [16] C. R. Algarín, J. T. Giraldo, and O. R. Álvarez, "Fuzzy logic based MPPT controller for a PV system," *Energies*, vol. 10, no. 12, p. 2036, 2017.
- [17] W. Hou, Y. Jin, C. Zhu, and G. Li, "A novel maximum power point tracking algorithm based on glowworm swarm optimization for photovoltaic systems," *International Journal of Photoenergy*, vol. 2016, Article ID 4910862, 9 pages, 2016.
- [18] Z. Qi and G. M. Koenig Jr., "Review article: flow battery systems with solid electroactive materials," *Journal of Vacuum Science & Technology B, Nanotechnology and Microelectronics: Materials, Processing, Measurement, and Phenomena*, vol. 35, no. 4, article 040801, 2017.
- [19] S. Dearborn, "Charging Li-ion batteries for maximum run times," *Power Electronics Technology*, vol. 31, no. 4, pp. 40–49, 2005.
- [20] T. Instruments, *INA219 Zero-Drift, Bidirectional Current/Power Monitor with I<sup>2</sup>C Interface*, Texas Instruments, 2015.
- [21] Aerosemi, *MT3608 High Efficiency 1.2MHz 2A Step Up Converter*, Aerosemi, 2015.
- [22] B. Hauke, *Basic Calculation of a Buck Converter's Power Stage*, Texas Instruments, Application Report, SLVA477B, 2011.
- [23] B. Bidoggia, *Notes on Design and Analysis of DC/DC Converters*, Department of Energy Technology, Aalborg University, Denmark, 2014.
- [24] R. L. Boylestad, *Electronic Devices and Circuit Theory*, Pearson Education India, 2009.
- [25] N. H. Weste and K. Eshraghian, "Principles of CMOS VLSI design: a systems perspective," NASA STI/Recon Technical Report A, 1985.
- [26] Multicomp Premier Farnell, *2n2222 Low Power Bipolar Transistor*, Multicomp Premier Farnell, 2016.
- [27] Arduino, "Secrets of Arduino PWM," April 2019, <https://www.arduino.cc/en/Tutorial/SecretsOfArduinoPWM>.
- [28] National Instrument, "What is Multisim," May 2019, <https://www.ni.com/en-us/shop/electronic-test-instrumentation/application-software-for-electronic-test-and-instrumentation-category/what-is-multisim.html>.

## Research Article

# High-Performance Emulator for Fixed Photovoltaic Panels

Youssef Mallal , Lhoussain El Bahir , and Touria Hassboun 

Laboratory of Electrical Engineering and Control Systems (LGECOS), National School of Applied Sciences, Cadi Ayyad University, Av. Abdelkrim El Khattabi B.P. 575, 40000 Marrakech, Morocco

Correspondence should be addressed to Youssef Mallal; mallalyoussef52@gmail.com

Received 8 July 2019; Accepted 9 September 2019; Published 14 October 2019

Guest Editor: Johnny P. Contreras

Copyright © 2019 Youssef Mallal et al. This is an open access article distributed under the Creative Commons Attribution License, which permits unrestricted use, distribution, and reproduction in any medium, provided the original work is properly cited.

This paper presents the design and implementation of a photovoltaic emulator, based on an accurate mathematical model of a photovoltaic panel, instead of the look-up table method. The latter requires more memory for increasing accuracy and considering all the desired environmental situations. Furthermore, the proposed approach takes into account the incidence solar angle, as an input parameter, to offer the possibility of evaluating daily losses for different values of tilt angle. The validation of the proposed emulator is carried out by comparing in real-time, both the studied panel output and the emulator output, under variable load, temperature, and irradiation levels. The emulator is able to operate online with connected solar radiation and temperature sensors or offline with recorded measurement vectors. The practical tests were performed on a prototype designed using a MATLAB C MEX S-function, dSPACE board 1104, and a controlled DC/DC converter. The results showed that the emulator was able to behave accurately as the studied photovoltaic panel.

## 1. Introduction

Photovoltaic emulators are nowadays becoming an alternative solution for indoor studying and analysing of photovoltaic systems. Recall that, those electronic power devices are able to reproduce the electrical behaviour of photovoltaic panels under controllable conditions.

In the literature, several methods to emulate photovoltaic panel behaviour have been studied. The reference generation could be analogue or digital; in [1, 2], two analogue reference generations were presented. The photovoltaic emulator developed in [1] consists in amplifying a photodiode I-V characteristic, which is considered as a PV cell. This method needs a light-emitting diode to simulate solar irradiation. Temperature control is ensured by a temperature controller of the photodiode. The authors in [2] have proposed a method to emulate the photovoltaic panel behaviour based on a logarithmic amplifier, operational amplifiers, variable resistors, adjustable linear voltage regulator, and a DC power supply. Although the analogue methods do not have a calculation delay, they are not flexible when controlling temperature and irradiation levels. An alternative solution is using digital reference generation combined with a power con-

verter. In the literature review, different digital controllers were used, namely, the microcontroller [3], the field-programmable gate array (FPGA) [4], and the digital signal processor (DSP) [5]. A hybrid digital-analogue reference generation is presented in [6].

A photovoltaic emulator can be considered as a controlled DC power supply able to reproduce photovoltaic panel characteristics, regardless of the environmental conditions. The general architecture of the PV emulator is shown in Figure 1.

It consists of three main elements: PV model implementation, control strategy, and power stage control [7]. The PV model reproduces the photovoltaic panel characteristic to be emulated; it receives as inputs, the temperature and the radiation in addition to measured photovoltaic panel voltage or current, according to the control type used for the power converter, current controlled or voltage controlled. The control strategy is the stage between the PV model and the power converter. It determines the intersection point between the photovoltaic emulator characteristic and the load characteristic. The power converter could be a linear regulator, a switching mode power supply, or a programmable DC power supply including the closed-loop control. The switching

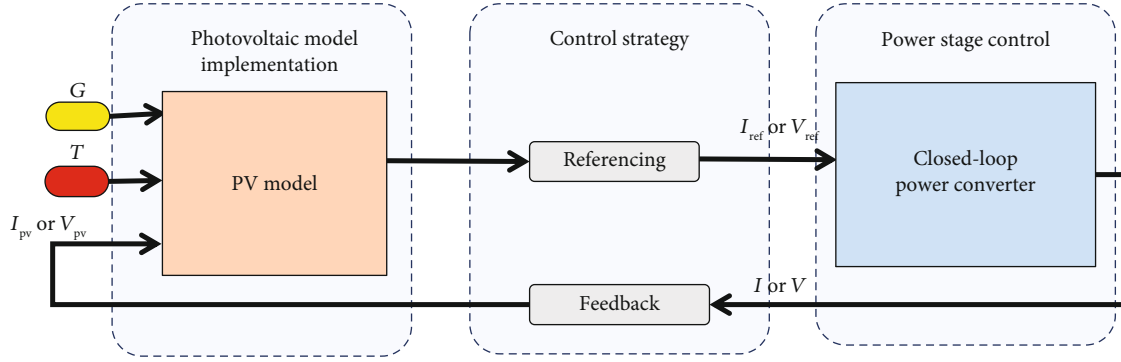


FIGURE 1: General photovoltaic emulator architecture.

mode power supplies are recommended for high-power applications, due to their efficiency and fast dynamic response.

Despite all the studies carried out for the design and implementation of photovoltaic emulators, the existing structures do not take into account all the operating conditions of solar panels, such as the geographical position, time, tilt angle of photovoltaic panels, and wind effect.

In this paper, we propose a new architecture of the photovoltaic emulator able to study the electrical characteristics of fixed photovoltaic installations, by considering time, tilt angle, latitude, and longitude as additional input parameters. The proposed emulator can also be used for loss estimation or tilt angle optimization. The control algorithm is implemented using a flexible direct calculation method to cover all temperature and irradiation levels. The design and the implementation are carried out on the dSPACE 1104 controller board. The DC/DC converter is designed to support the current delivered by the SR-20 panel under different operating conditions. One of the strong points of the proposed emulator is the ability to reproduce, in real-time, a very accurate electrical power, synchronously with a reference PV panel under real weather conditions and variable load. The results showed a good agreement between the emulator and the panel responses in transient and steady states.

The rest of the paper is organized as follows. The proposed emulator implementation is given in Section 2; the model of the photovoltaic panel and its practical validation are presented in Section 3. Section 4 is dedicated to the design and control strategy of the power converter. Section 5 presents real-time implementation results and analysis. Finally, some concluding remarks and perspectives are presented in the last section.

## 2. Structure of the Proposed Photovoltaic Emulator

Photovoltaic emulators developed in the literature emulate the photovoltaic panel behaviour at the desired temperature and solar irradiation. The latter is influenced by the incidence angle of the sunrays, which represents the angle between the sunlight and the normal to the surface of the panel. The reflected and diffuse solar radiations can be neglected

compared to the direct solar radiation  $G_D$ . The effective solar radiation  $G_i$  received by the panel for a given incidence angle  $i$ , is given by [8]:

$$G_i = \cos(i) \times G_D. \quad (1)$$

The incidence angle of solar radiation on an inclined panel depends on several angles. The illustration of these angles is presented in Figure 2, where BO is the normal to the horizontal surface, CO is the normal to the tilt surface, OE is the projection of the normal to the inclined surface on the horizontal plane,  $\gamma$  is the surface azimuth angle, and  $\beta$  is the tilt angle, measured from the horizontal. By applying cosine law on various mentioned above angles, one can deduce the following relationships [9]:

$$\cos(i) = \cos(\beta) \cos(z) + \sin(\beta) \sin(z) \cos(\alpha - \gamma),$$

$$\sin(\alpha) = \frac{\sin(\omega) \cos(\delta)}{\sin(z)},$$

$$\cos(z) = \sin(\delta) \sin(\phi) + \cos(\delta) \cos(\phi) \cos(\omega),$$

$$\delta = 23.45^\circ \sin\left[\frac{360}{365}(284 + d)\right],$$

$$\omega = (ST - 12) \times 15^\circ,$$

$$ST = t + ET \pm 4(L_{ST} - L) + DST,$$

$$L_{ST} = 15^\circ \Delta GMT,$$

$$ET = 229.2(0.000075 + 0.001868 \cos(B) - 0.032077 \sin(B) - 0.014615 \cos(2B) - 0.04089 \sin(2B)),$$

$$B = (d - 1) \frac{360}{365},$$

(2)

where  $z$  is the zenith angle,  $\phi$  is the latitude,  $\alpha$  is the solar azimuth angle,  $\delta$  is the declination angle,  $d$  is the day of the year,  $\omega$  is the solar hour angle, ST is the solar time,  $L_{ST}$  is the local standard time meridian, LT is the local time, GMT is the Greenwich Mean Time, in hours,  $\Delta GMT$  is the difference of

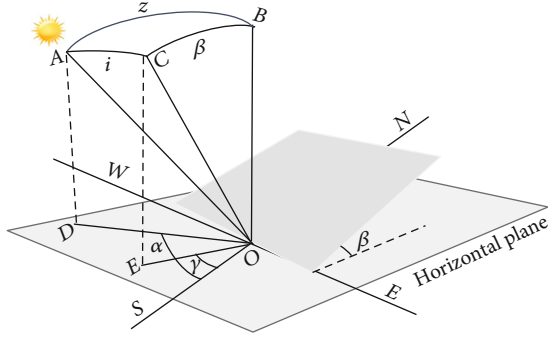


FIGURE 2: Solar radiation on tilt photovoltaic panel.

LT and GMT,  $L$  is the longitude, ET is the equation time, DST is the daylight saving time, and  $t$  is the standard time.

The incidence angle in terms of declination angle, tilt angle, latitude, and hour angle is given by:

$$\begin{aligned} \cos(i) = & \sin(\delta)[\sin(\phi)\cos(\beta) - \cos(\phi)\sin(\beta)] \\ & + \cos(\delta)\cos(\omega)[\cos(\phi)\cos(\beta) \\ & + \sin(\phi)\sin(\beta)\cos(\gamma)]. \end{aligned} \quad (3)$$

When the inclined photovoltaic panel faces the equator ( $\gamma = 0$ ), equation (3) becomes

$$\begin{aligned} \cos(i) = & \sin(\delta)[\sin(\phi)\cos(\beta) - \cos(\phi)\sin(\beta)] \\ & + \cos(\delta)\cos(\omega)[\cos(\phi)\cos(\beta) + \sin(\phi)\sin(\beta)]. \end{aligned} \quad (4)$$

Hence,

$$\cos(i) = \sin(\phi - \beta)\sin(\delta) + \cos(\phi - \beta)\cos(\delta)\cos(\omega). \quad (5)$$

The developed emulator architecture is shown in Figure 3.

According to equation (1), the cosine of the incidence angle is multiplied by the solar radiation to calculate the actual value of solar radiation received by the panel, under the installation conditions. From the user-defined inputs and the measured voltage  $V_{pve}$ , considered as the emulator voltage, the PV model generates a current reference  $I_{ref}$  that will be compared with the current-controlled buck converter output  $I_{pve}$ , considered as the emulator current. The error is minimized by the PI controller to maintain  $I_{pve}$  to its reference value  $I_{ref}$ . The model and control algorithm are programmed under MATLAB/Simulink and loaded on the dSPACE controller board. The LEM LA55-P and the LEM LV20-P are, respectively, the current and the voltage sensors. Their outputs are connected to a conditioning circuit to deliver a voltage between 0 and  $\pm 10$  volts, adapted as an input of the dSPACE board ADC.

The dSPACE board contains a Master Floating-Point DSP (400 MHz) for processing and a Slave DSP (20 MHz) for controlling PWM and digital I/Os. The control parameters, the sensor gains, and the data visualization are carried out under ControlDesk software.

The major targeted goals, during the development of this architecture, are (i) the design of a photovoltaic emulator with the same response as a photovoltaic panel in the transient and steady state, (ii) considering the actual installation conditions of photovoltaic panels. (iii) The emulator must be able to operate in real-time with connected temperature and radiation sensors or with stored data from other stations, (iv) a simple and accurate control law easy to be implemented in other platforms. The details of the implementation and design of each part of the architecture are given in the following sections.

### 3. Photovoltaic Panel Model Implementation

A photovoltaic cell is an electric power generator, consisting of semiconductor layers that convert solar energy into electricity. Depending on the load connected to its terminals, it can behave as a current source or as a voltage source [10]. In the literature review, several photovoltaic models are used to simulate the photovoltaic panel behaviour. They are divided into two categories: electrical circuit models based on the electrical characteristics of the photovoltaic panel and interpolation models based on the IV characteristic of the photovoltaic panel [11]. Even if the electrical circuit models are less fast compared with the linear models, they are commonly used by the researchers, due to their accuracy. The most popular electric models are the double diode model and the single diode model. The latest presents a good compromise between accuracy and simplicity [12]. The photovoltaic model implementation is carried out by several methods, direct calculation method, look-up table method, piecewise-linear method, neural network method, and photovoltaic elimination voltage method [7]. The direct calculation method is characterized by good accuracy and low memory demand. In this paper, we used an electric model (1D2R) with a numerical calculation method to avoid the use of look-up tables to increase the model accuracy. The 1D2R model with the equivalent circuit is shown in Figure 4.

The current-voltage characteristic of a photovoltaic module is represented by equation (8).

$$I = I_{ph} - I_D - I_p, \quad (6)$$

where

$$\begin{aligned} I_D = & I_0(e^{V/AV_t} - 1), \\ I_p = & \frac{V + R_s I}{R_p}. \end{aligned} \quad (7)$$

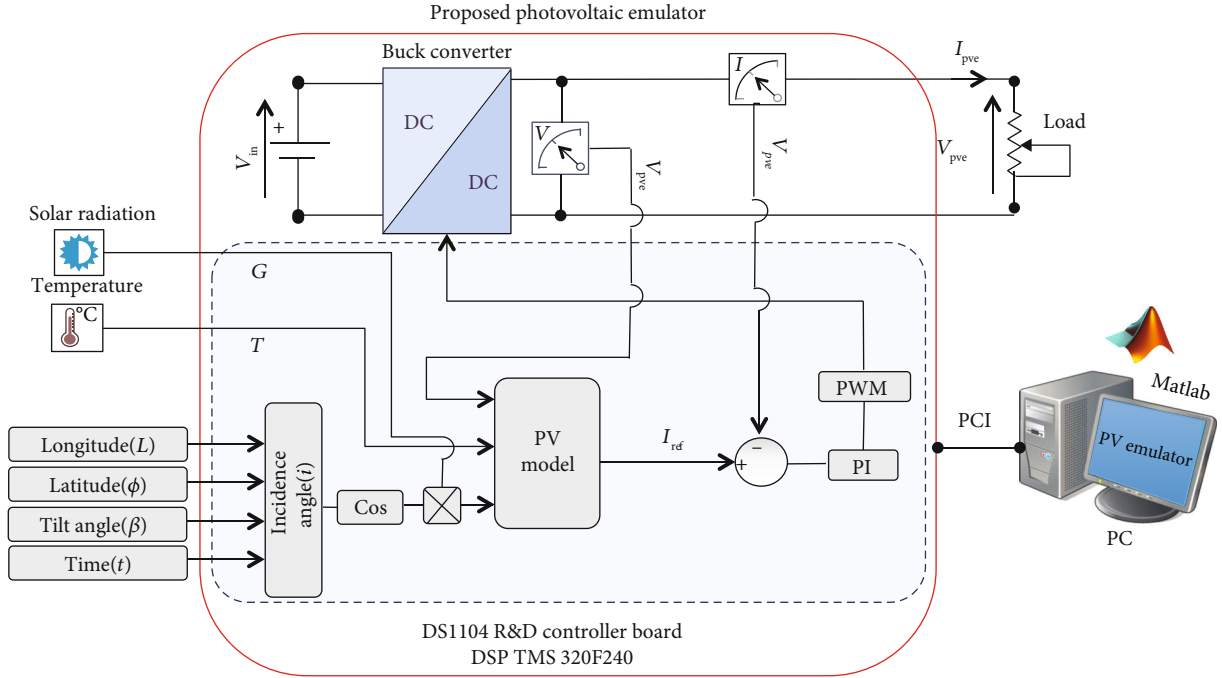


FIGURE 3: Proposed photovoltaic emulator architecture.

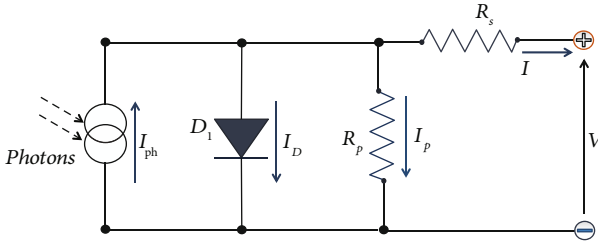


FIGURE 4: Equivalent circuit model of the 1D2R model.

Hence,

$$I = I_{ph} - I_0 \left( e^{\left( \frac{V + R_s I}{V_t A} \right)} - 1 \right) - \frac{V + R_s I}{R_p}. \quad (8)$$

The current  $I_{ph}$  describes the photogenerated current of the photovoltaic panel; it depends on solar radiation and temperature as follows:

$$I_{ph} = \frac{G}{G_n} [I_{scr} + K_i (T - T_r)]. \quad (9)$$

$V_t = kTc/q$  is the thermal voltage,  $k$  is the Boltzmann constant,  $T$  is the temperature of the photovoltaic panel and  $A$  is the diode ideality factor,  $q$  is the electronic charge,  $T_r$  is the reference temperature,  $I_{scr}$  is the short circuit current at  $T_r$ ,  $K_i$  is the short circuit current/temperature coefficient, and  $G_n$  is the nominal irradiation.

The reverse saturation current of diode  $I_0$  may be expressed by

$$I_0 = I_n \left( \frac{T_c}{T_r} \right)^3 e^{(qE_g/Ak) \left( \frac{1}{T_r} - \frac{1}{T_c} \right)}, \quad (10)$$

where  $I_n$  is the nominal saturation current and  $E_g$  is the band gap energy.

The identification of the unknown parameters mentioned above is based on the physical parameters of the studied panel, given in the manufacturer's datasheet at standard test conditions (STCs) of temperature and solar irradiation. The specifications of the SR-20 panel are given in Table 1.

The model is programmed as a C MEX S-Function and loaded on the dSPACE 1104 controller board. Firstly, the model is validated in simulation as shown in Figure 5.

As can be seen in Figure 5, the simulated current-voltage and power-voltage characteristics, under nominal conditions of temperature and irradiation, reproduce the same values of  $V_{OC}$ ,  $I_{SC}$ ,  $V_{MP}$ , and  $I_{MP}$ . The model is also validated with real data of irradiation and temperature recorded for short cloudy periods. The results of this validation have shown that the model behaves exactly as the SR-20 panel, under variable conditions of temperature and irradiation, as shown in Figure 6.

#### 4. Power Stage Design and Control

There are three main power converters used in photovoltaic emulator applications: linear regulator [1], programmable DC power supply [13], and Switching-Mode Power Supply

TABLE 1: SR-20 PV panel specifications (A.M.1.5,  $1 \text{ kW/m}^2$ ,  $25^\circ\text{C}$ ) and identified parameters of the adjusted model.

Voltage at MPP ( $V_{MP}$ )	17.2 V
Current at MPP ( $I_{MP}$ )	1.17 A
Short circuit current ( $I_{SC}$ )	1.28 A
Open circuit voltage ( $V_{OC}$ )	21.6 V
Maximum power ( $P_{MP}$ )	20 W
Ideality factor ( $A$ )	1.9
Charge of electron ( $q$ )	$1.6e-19 \text{ C}$
Boltzmann constant ( $k$ )	$1.38e-23 \text{ J/K}$
Band gap energy ( $E_g$ )	1.12 eV
Reverse saturation current at $T_r$ ( $I_n$ )	$5.98e-6 \text{ A}$
Temperature coefficient of SC current ( $K_i$ )	$512.10e-6 \text{ A/K}$
Number of cells connected in series ( $n_s$ )	36
Number of cells connected in parallel ( $n_p$ )	1
Internal series resistance of a cell ( $R_s$ )	$0.004 \Omega$
Internal parallel resistance of a cell ( $R_p$ )	$1000 \Omega$

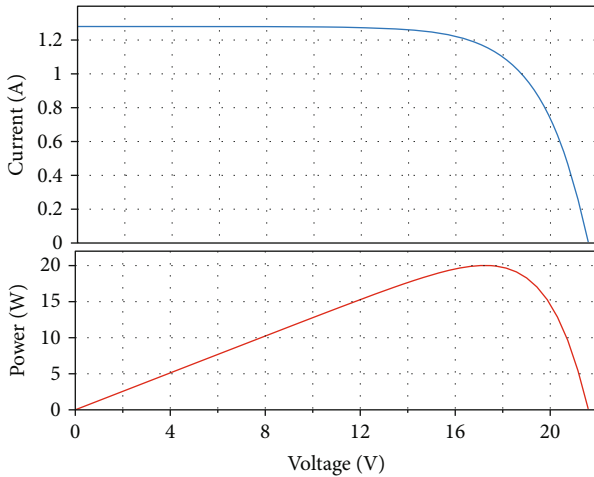


FIGURE 5: I-V and P-V characteristics of the PV panel at  $1000 \text{ W/m}^2$ ,  $T = 25^\circ\text{C}$ .

(SMPS) [4]. Since the efficiency of the linear regulator is low, it is rarely used in photovoltaic emulator applications. The programmable DC power supply includes the closed-loop control, but it suffers from the response delay. As a result, the SMPS is more suitable for photovoltaic emulators in terms of efficiency and dynamic response. Among the common SMPS topologies, a buck converter is used to cover the values of the emulated panel I-V characteristic. The control type is current control, ensured by a PI controller. The electrical circuit of the buck converter is shown in Figure 7, operating in the continuous conduction mode (CCM). The design parameters are given in Table 2.

The selection of the values of  $C$  and  $L$  is based on the standard design equations. The DC-DC buck converter was

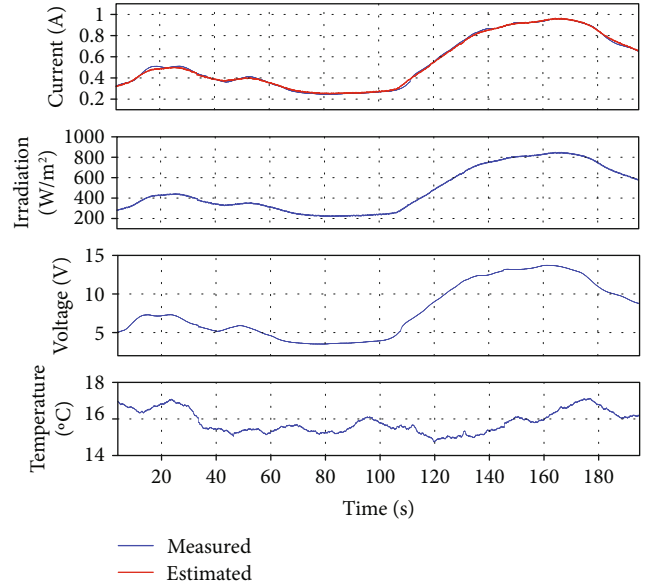


FIGURE 6: Model validation under natural conditions.

built using IRF540NPBF MOSFET connected to FOD3120 gate driver. The selected values of  $L$  and  $C$  are  $1 \text{ mH}$  and  $470 \mu\text{F}$ , respectively.

The closed-loop control is shown in Figure 8. It consists of a PI controller receiving the current reference from the PV model. The buck converter is current-controlled. Its transfer function, derived from the small-signal analysis, is given by [7]:

$$G_{\text{BUCK}}(s) = \frac{\hat{i}_{\text{pve}}(s)}{\hat{d}(s)} = \frac{V_{\text{in}}/R}{LCs^2 + (L/R)s + 1}. \quad (11)$$

The second-order term coefficient,  $LC$ , could be neglected ( $LC \sim 1e-7$ ) compared to  $L/R$  ( $L/R \sim 1e-3$ ). The system can then be considered as a first-order system, equation (22).

$$G_{\text{BUCK}}(s) = \frac{\hat{i}_{\text{pve}}(s)}{\hat{d}(s)} = \frac{V_{\text{in}}/R}{(L/R)s + 1}. \quad (12)$$

The PI parameters are tuned to ensure a fast response, stability, and minimizing steady-state error. The closed-loop responses for abrupt load and setpoint changes are given in Figure 9. As can be seen, the designed controller is able to track the setpoint  $I_{\text{ref}}$  regardless of load and reference change conditions.

As mentioned previously, the control strategy plays a very important role in the determination of the operating point. There are several control strategies of photovoltaic emulators reported in the literature, namely, the resistance comparison method [14], the hill-climbing method [15], the hybrid-mode controlled method [16], and the direct referencing method [7]. In this study, we used a direct referencing method that works with the SMPS and does not



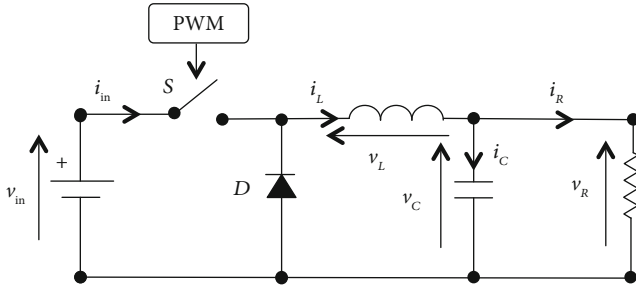


FIGURE 7: Buck converter architecture.

TABLE 2: Design parameters of buck converter.

Input voltage ( $V_{in}$ )	24 V
Switching frequency ( $f_{SW}$ )	20 kHz
Output voltage ripple ( $\Delta V$ )	10 mV
Inductor current ripple ( $\Delta I$ )	30%

require any additional algorithm. This method involves connecting the emulator output voltage  $V_{pve}$  to the PV model input. The latter generates a current reference  $I_{ref}$  applied to the PI controller input, Figure 8.

At the start time, the  $V_{pve} = 0$  and the photovoltaic model generates a reference current  $I_{ref} = I_{sc}$ , for a given load, irradiance, and temperature. As  $V_{pve}$  increases,  $I_{ref}$  begins to decrease following the PV panel I-V characteristic. The PV emulator stabilizes on an operating point when  $V_{pve}$  and the output current  $I_{pve}$ , correspond to the output resistance  $R_{Load}$  on the I-V characteristic, Figure 10.

## 5. Results and Discussion

Unlike previous works in this domain, the superiority of the method in real-time processing was experimentally validated by connecting the photovoltaic panel and the emulator to two similar resistive loads and comparing simultaneously both panel and emulator outputs. Under the same variable conditions of temperature, solar radiation, load, latitude, longitude, time, and tilt angle, the emulator must be able to deliver the same voltage and current as the SR-20 solar panel. The scheme of the practical platform is illustrated in Figure 11.

A photograph of the experimental platform, with its instrumentation, is shown in Figure 12. The solar radiation, current, voltage, and temperature are, respectively, measured by CM10, LEM LA55-P, LEM LV20-P, and PT1000 sensors. The signals pass through a conditioning circuit to deliver voltages between 0 and  $\pm 10$  volts, adapted to ADC inputs of the dSPACE controller board. The photovoltaic emulator was tested under variable load, solar radiation, and temperature. The validation results are given in the next subsections.

Experimental tests were carried out during alternating sunny and cloudy periods, in Marrakech on April 2nd,

2019, from 14 h 30 mins to 17 h 30 mins. The SR-20 panel is fixed in a position of 31 degrees facing south. The validation was carried out progressively, by first individually testing the effect of each of the factors, including load, irradiation, and temperature and secondly the simultaneous variation of the different factors, taking into account the effect of the solar incidence angle studied in Section 2.

**5.1. Electrical Characteristic Verification.** To demonstrate the validity of the proposed emulator, it would be appropriate to start with standard offline tests, based on controlled  $G$  and  $T$  variations. To generate the I-V characteristics, the proposed emulator was connected to a variable load, for different values of solar radiation and temperature. The comparison between the obtained I-V characteristics and those of the reference panel is given in Figure 13. Test results have shown that the proposed emulator behaves exactly like the SR-20 panel, throughout the I-V characteristic.

Since the incidence angle is related to real-time operation of the PV system, the integration of its effect on the emulator is validated subsequently.

**5.2. Load Variation.** When changing the load, the emulator and the photovoltaic panel are each connected to three resistive loads ( $19 \Omega$ ,  $15 \Omega$ , and  $9 \Omega$ ); switching from one load to another is carried out, simultaneously, by controlled relays. Figure 14 illustrates the behaviour of the emulator and panel under load variation and during a period when the temperature and irradiation are considered constant. As can be seen from the curve, the emulator faithfully reproduces the same electrical behaviour as the SR-20 panel.

**5.3. Irradiation Variation.** The effect of variable irradiation at stable temperature (at  $29^\circ\text{C}$ ) is shown in Figure 15. The tests are performed under periods of dense and less dense clouds, inducing a variation of solar irradiation between  $375 \text{ W/m}^2$  and  $627 \text{ W/m}^2$ . The results showed that the emulator was able to follow accurately abrupt changes in irradiation with a high robustness degree.

**5.4. Simultaneous Variation of Load and Environmental Conditions.** In natural operation, photovoltaic panels work under uncontrollable environmental and load conditions. A powerful emulator should be able to reproduce the same electrical behaviour as a photovoltaic panel under such conditions. The test conditions are shown in Figure 16. As can be seen, the emulator behaves in a very efficient way throughout the test, in particular, the area between 15 and 25 mins where the three factors vary at the same time.

**5.5. Incidence Angle Effect.** To study the electrical behaviour of a fixed installation through an emulator, it would be appropriate to consider the incidence angle effect on the electrical photovoltaic panel characteristic. In about 20 mins, between 14 h 30 mins and 14 h 50 mins, the incidence angle presents a variation of more than 3 degrees, leading to a progressive output emulator error. At 14 h 50 mins, an adjustment of the incidence angle was introduced in the emulator input, as shown in Figure 17.

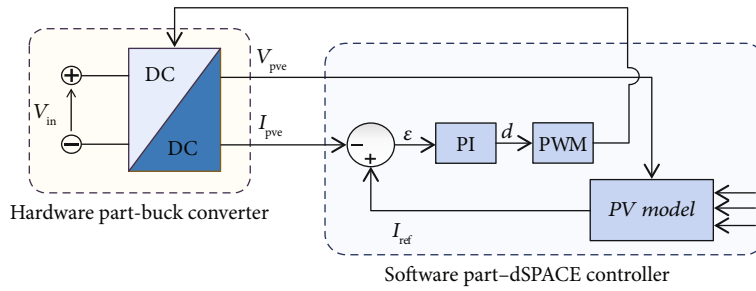


FIGURE 8: Power stage closed-loop control.

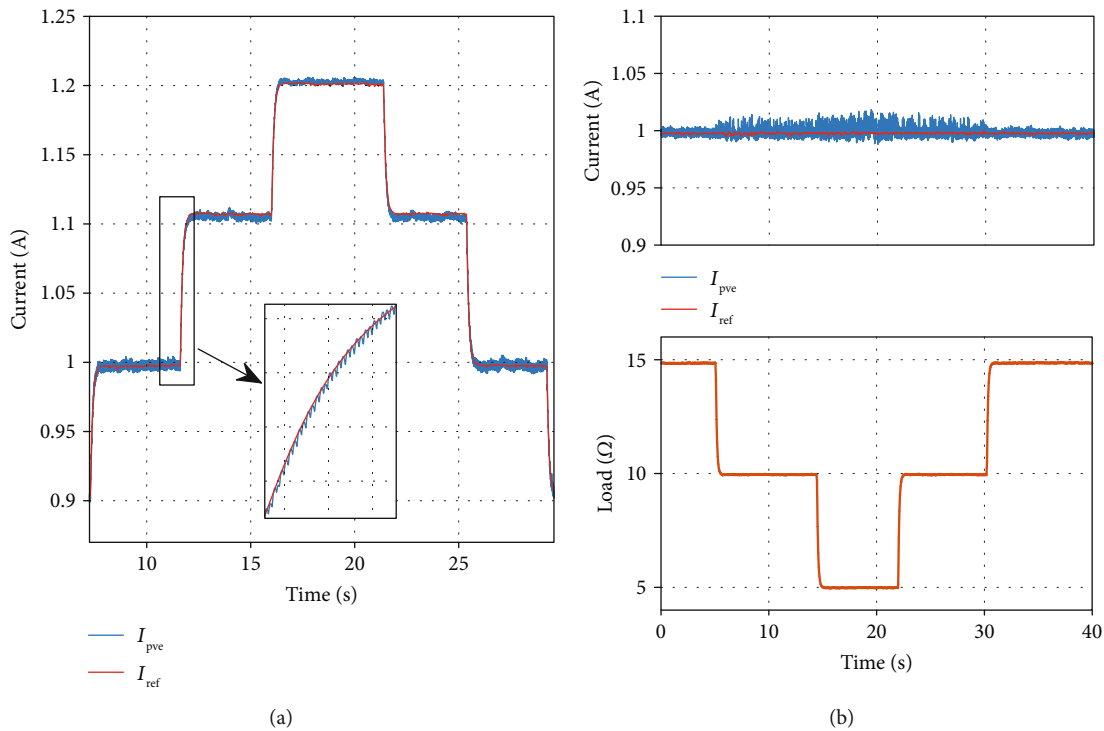


FIGURE 9: (a) Closed-loop response for abrupt setpoint change, (b) closed-loop response for abrupt load change.

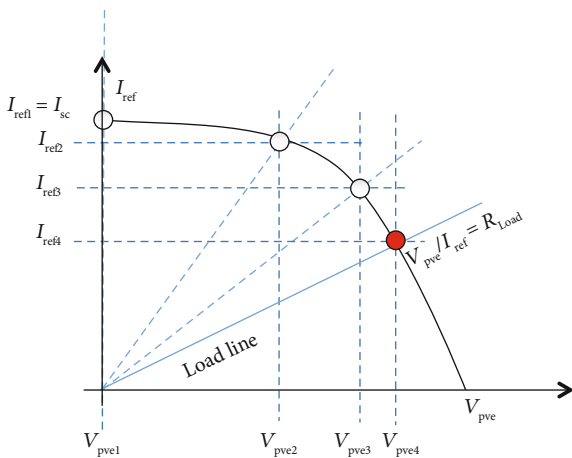


FIGURE 10: Control strategy principle.

An overall summary test was performed in real-time on a fixed panel for 2 h 30 mins, to highlight the performance of our emulator for the final prototype, Figure 18. During the test, the solar irradiation and the temperature show significant natural variations. The load varies arbitrarily between 19 Ω, 15 Ω, and 9 Ω. The emulator combines the measured solar irradiation with an estimated incidence angle to determine the actual irradiation received by the panel. The incidence angle changes from 49° to 82°. The current and the voltage generated by the emulator, under the same conditions, show a perfect agreement with those delivered by the photovoltaic panel under consideration.

## 6. Conclusion

In this paper, a prototype of a high-performance photovoltaic emulator has been developed, including the effect

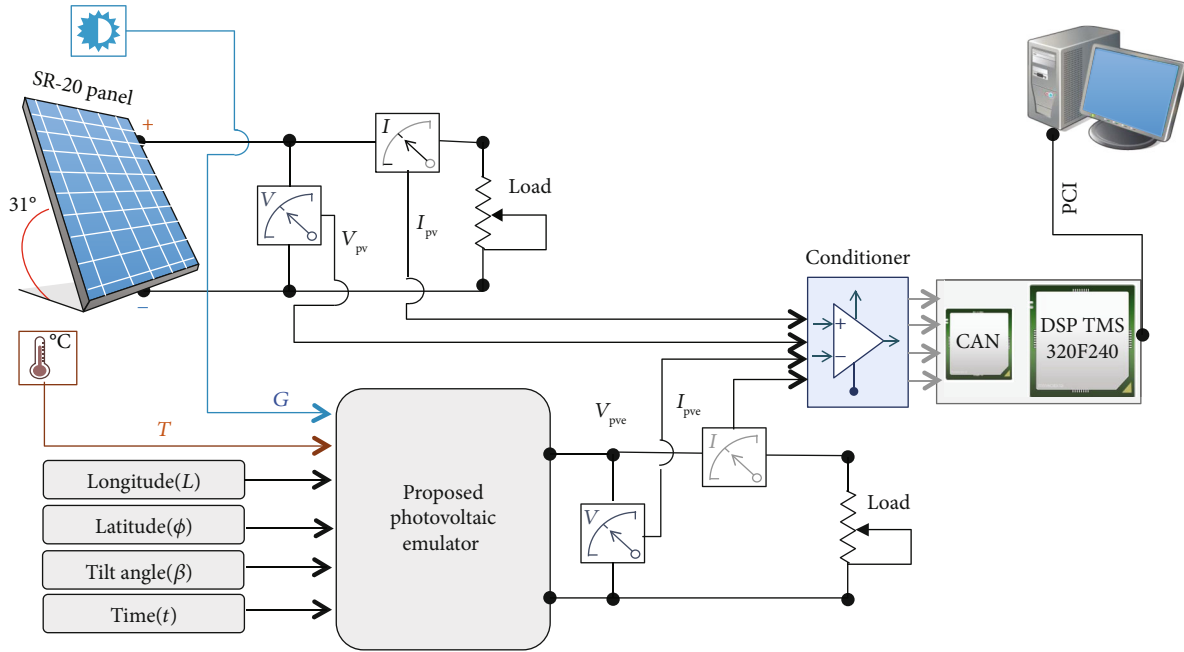


FIGURE 11: Experimental validation scheme.

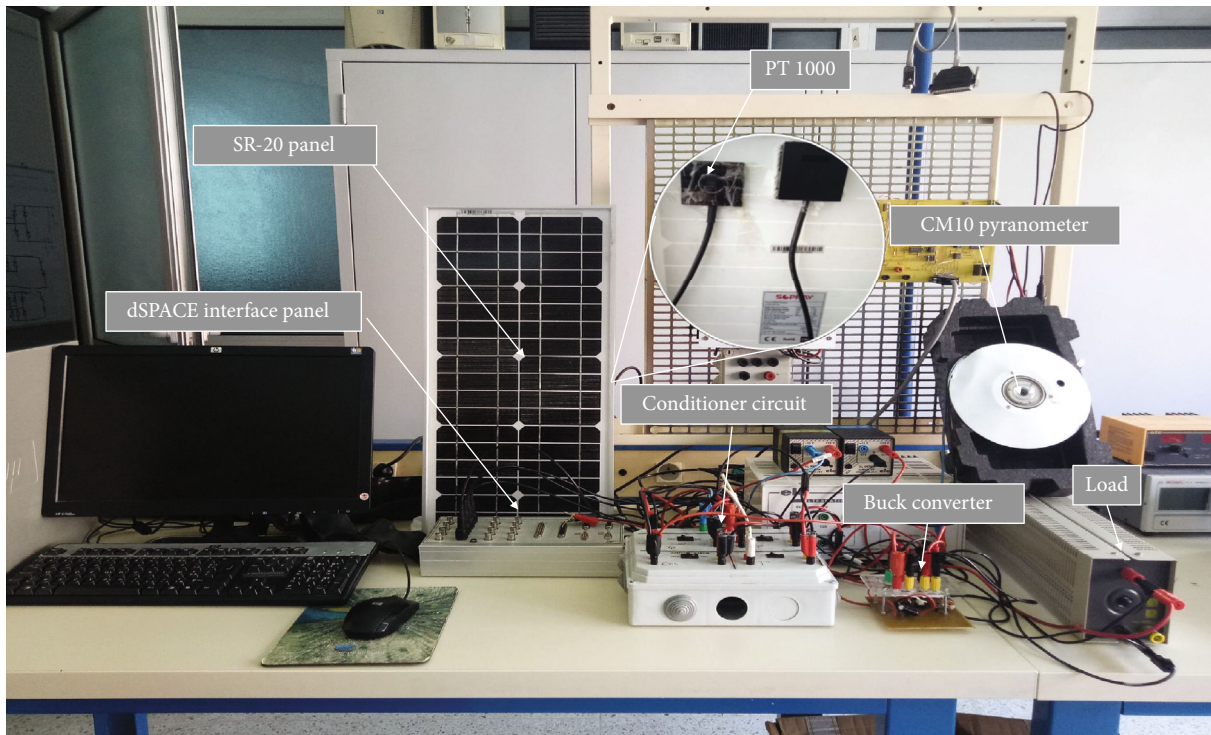


FIGURE 12: A photograph of the experimental platform.

of the incidence angle. The experimental validation was carried out in real-time, by comparing both panel and emulator outputs.

As the converter is a key element in the emulator architecture, special attention has been given to its control system

to maintain the same performance for any operating point. The proposed control algorithm is based on an autotuning PI controller, according to load and input voltage variations. The method leads to a simple and accurate control law easy to implement on any digital platform.

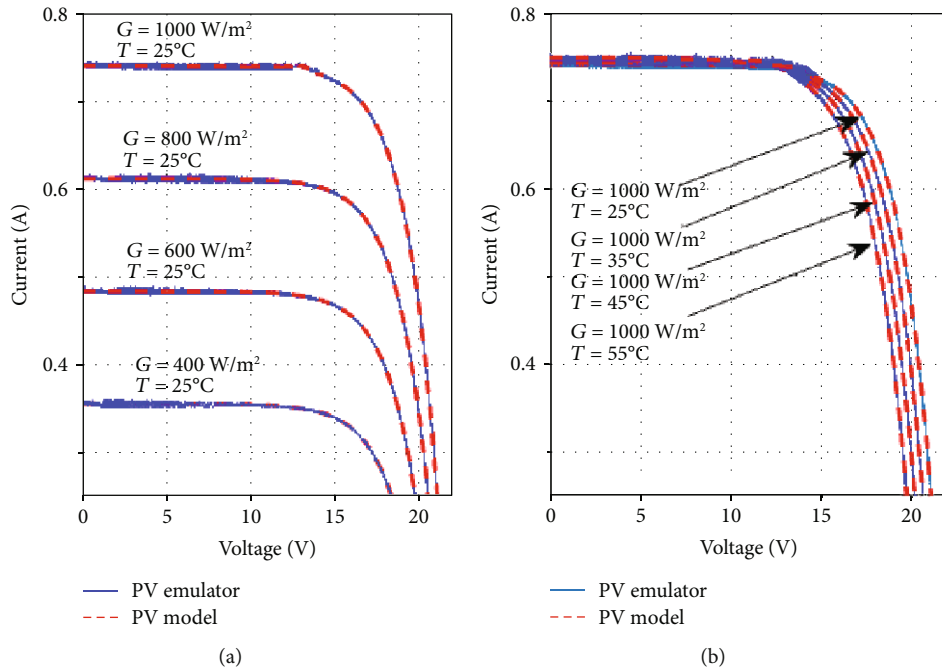


FIGURE 13: (a) Generated I-V characteristics for a fixed temperature and variable solar radiation, (b) generated I-V characteristics for a variable temperature and fixed solar radiation.

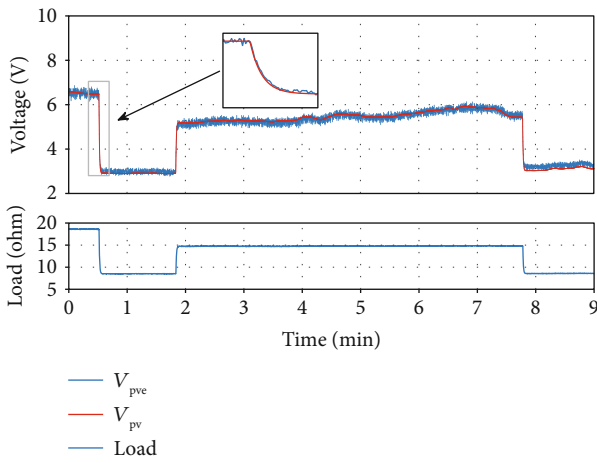


FIGURE 14: Proposed emulator test under load variation.

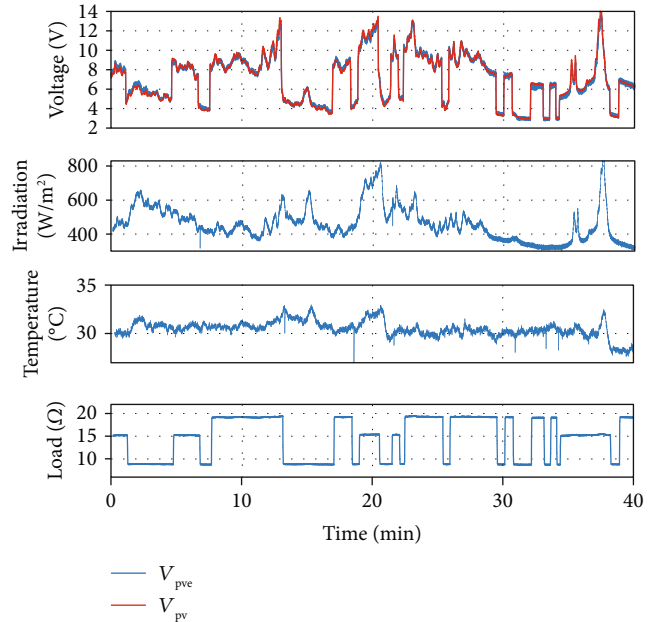


FIGURE 16: Proposed emulator test under simultaneous variation of load and environmental conditions.

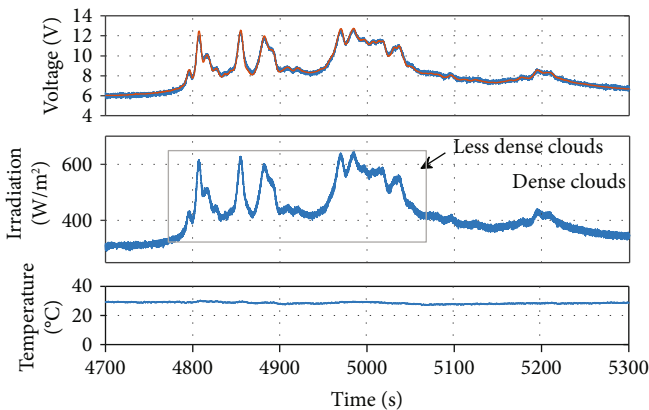


FIGURE 15: Proposed emulator test under variable irradiation.

To validate all expected performances of the proposed emulator structure, a practical platform has been designed and developed for this purpose. A global test scenario was used to validate the dynamic and steady-state responses of the emulator under realistic and possible operating conditions.

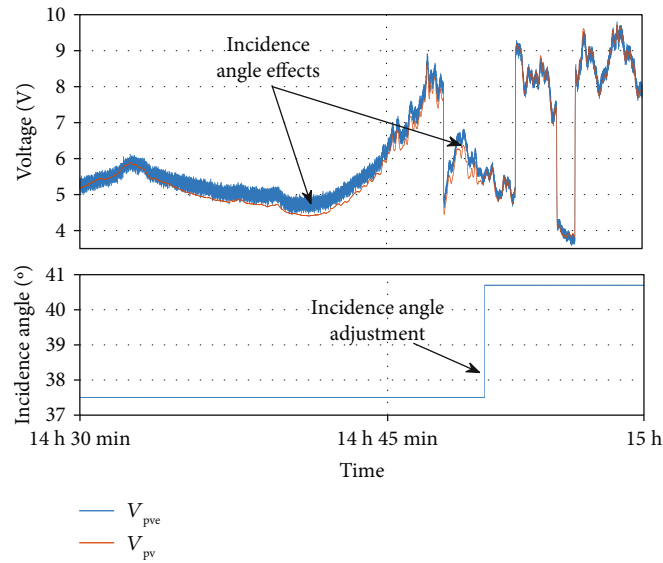


FIGURE 17: Incidence angle effect on emulator output.

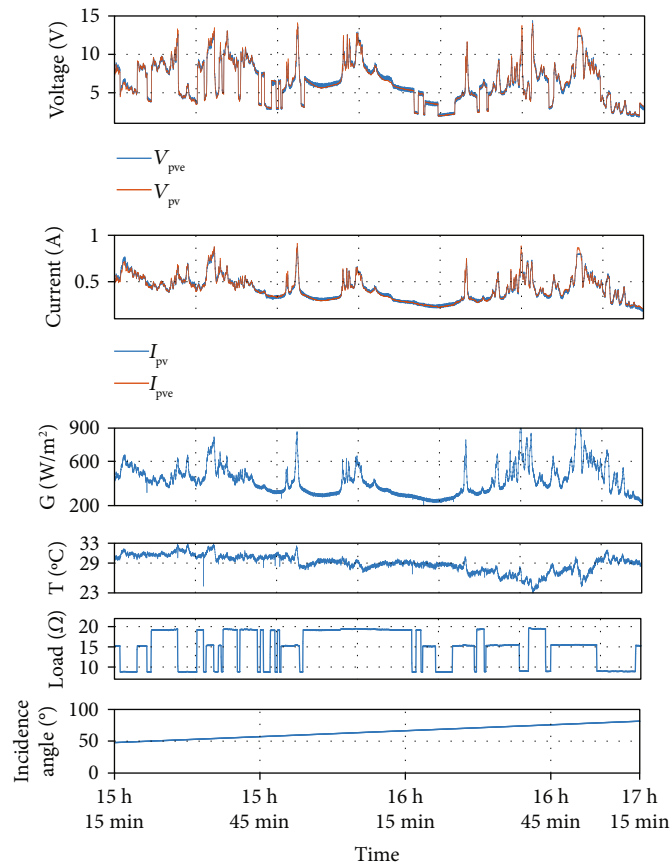


FIGURE 18: Proposed emulator test under real use conditions with automatic incidence angle adjusting.

The obtained results showed that the emulator could behave accurately as the reference photovoltaic panel under variable environmental conditions and load abrupt changes. The results showed also that for a fixed panel

the emulator considers efficiently the daily incidence angle evolution.

A hardware platform based on a low-cost digital controller is under development.

## Data Availability

The data used to support the findings of this study are available from the corresponding author upon request.

## Conflicts of Interest

The authors declare that they have no conflicts of interest.

## References

- [1] I. Moussa, A. Khedher, and A. Bouallegue, "Design of a low-cost PV emulator applied for PVECS," *Electronics*, vol. 8, no. 2, p. 232, 2019.
- [2] H. Nagayoshi, "I-V curve simulation by multi-module simulator using I-V magnifier circuit," *Solar Energy Materials and Solar Cells*, vol. 82, no. 1-2, pp. 159–167, 2004.
- [3] C. Balakishan and S. Babu, "Development of a microcontroller based PV emulator with current controlled DC/DC buck converter," *International Journal of Renewable Energy Research*, vol. 4, no. 4, pp. 1049–1055, 2014.
- [4] D. Ickilli, H. Can, and K. S. Parlak, "Development of a FPGA-based photovoltaic panel emulator based on a DC/DC converter," in *2012 38th IEEE Photovoltaic Specialists*, pp. 001417–001421, Austin, TX, USA, 2012.
- [5] P. H. To and D. Q. Phan, "A photovoltaic emulator using dSPACE controller with simple control method and fast response time," in *2017 International Conference on System Science and Engineering (ICSSE)*, pp. 718–723, Ho Chi Minh City, Vietnam, 2017.
- [6] G. Vachtsevanos and K. Kalaitzakis, "A hybrid photovoltaic simulator for utility interactive studies," *IEEE Transactions on Energy Conversion*, vol. EC-2, no. 2, pp. 227–231, 1987.
- [7] R. Ayop and C. W. Tan, "A comprehensive review on photovoltaic emulator," *Renewable and Sustainable Energy Reviews*, vol. 80, pp. 430–452, 2017.
- [8] M. A. Ionita and C. Alexandru, "Simulation of a dual-axis tracking system for PV modules," *Bulletin of the Transilvania University of Brasov Engineering Sciences Series I*, vol. 4, no. 2, p. 45, 2011.
- [9] J. E. Braun and J. C. Mitchell, "Solar geometry for fixed and tracking surfaces," *Solar Energy*, vol. 31, no. 5, pp. 439–444, 1983.
- [10] T. Hassboun, L. El Bahir, Y. A. DRISS, and M. El Adnani, "Solar irradiation estimator based on a self-calibrated reference solar cell," *Turkish Journal of Electrical Engineering & Computer Sciences*, vol. 24, no. 6, pp. 4885–4899, 2016.
- [11] R. Ayop and C. W. Tan, "A comparison study of interpolation and circuit based photovoltaic mathematical models," in *2016 IEEE International Conference on Power and Energy (PECon)*, pp. 626–631, Melaka, Malaysia, 2016.
- [12] L. E. Bahir and T. Hassboun, "Accurate maximum power point tracking algorithm based on a photovoltaic device model," *International Journal of Photoenergy*, vol. 2017, Article ID 5693941, 10 pages, 2017.
- [13] A. F. Ebrahim, S. M. W. Ahmed, S. E. Elmasry, and O. A. Mohammed, "Implementation of a PV emulator using programmable DC power supply," in *SoutheastCon 2015*, pp. 1–7, Fort Lauderdale, FL, USA, 2015.
- [14] R. Ayop and C. W. Tan, "Improved control strategy for photovoltaic emulator using resistance comparison method and binary search method," *Solar Energy*, vol. 153, pp. 83–95, 2017.
- [15] J. Gonzalez-Llorente, A. Rambal-Vecino, L. A. Garcia-Rodriguez, J. C. Balda, and E. I. Ortiz-Rivera, "Simple and efficient low power photovoltaic emulator for evaluation of power conditioning systems," in *2016 IEEE Applied Power Electronics Conference and Exposition (APEC)*, pp. 3712–3716, Long Beach, CA, USA, 2016.
- [16] Y. Li, T. Lee, F. Z. Peng, and D. Liu, "A hybrid control strategy for photovoltaic simulator," in *2009 Twenty-Fourth Annual IEEE Applied Power Electronics Conference and Exposition*, pp. 899–903, Washington, DC, USA, 2009.